Mahoney, E. J. D., Mushtaq, S., Ashfold, M. N. R., & Mankelevich, Y. A. (2019). Combined Spatially Resolved Optical Emission Imaging and Modeling Studies of Microwave-Activated H_2/Ar and H_2/Kr Plasmas Operating at Powers and Pressures Relevant for Diamond Chemical Vapor Deposition. *Journal of Physical Chemistry A*, *123*(13), 2544-2558. https://doi.org/10.1021/acs.jpca.8b12294

Combined Spatially Resolved Optical Emission Imaging and Modeling Studies of Microwave-Activated H_2/Ar and H_2/Kr Plasmas Operating at Powers and Pressures Relevant for Diamond Chemical Vapor Deposition

Edward J.D. Mahoney,[1,2] Sohail Mushtaq,[1] Michael N.R. Ashfold [1]*
and Yuri A. Mankelevich [3]

[1] School of Chemistry, University of Bristol, Bristol, U.K. BS8 1TS

[2] Centre for Doctoral Training in Diamond Science and Technology, University of Warwick, Gibbet Hill Road, Coventry, U.K., CV4 7AL

[3] Skobel'tsyn Institute of Nuclear Physics, Lomonosov Moscow State University, Leninskie gory, Moscow, 119991 Russia

TOC graphic

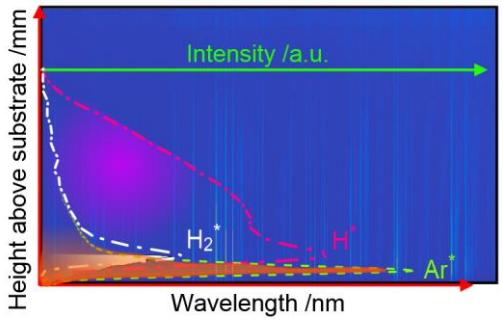
Intensity /a.u.
Height above substrate /mm
Wavelength /nm
H2*
H*
Ar*

Abstract

Microwave (MW) activated H_2/Ar (and H_2/Kr) plasmas operating under powers and pressures relevant to diamond chemical vapor deposition have been investigated experimentally and by 2-D modeling. The experiments return spatially and wavelength resolved optical emission spectra of electronically excited H_2 molecules and H and Ar(/Kr) atoms for a range of H_2/noble gas mixing ratios. The self-consistent 2-D(*r*, *z*) modeling of different H_2/Ar gas mixtures includes calculations of the MW electromagnetic fields, the plasma chemistry and electron kinetics, heat and species transfer and gas−surface interactions. Comparison with the trends revealed by the spatially resolved optical emission measurements and their variations with changes in process conditions help guide identification and refinement of the dominant plasma (and plasma emission) generation mechanisms and the more important Ar–H, Ar–H_2 and H–H_2 coupling reactions. Noble gas addition is shown to encourage radial expansion of the plasma, and thus to improve the uniformity of the H atom concentration and the gas temperature just above the substrate. Noble gas addition in the current experiments is also found to enhance (unwanted) sputtering of the copper base plate of the reactor; the experimentally observed increase in gas phase Cu* emission is shown to correlate with the near substrate ArH^+ (and KrH^+) ion concentrations returned by the modelling, rather than with the relatively more abundant H_3^+ (and H_3O^+) ions.

1. Introduction

Microwave (MW) plasma-enhanced chemical vapour deposition (PE CVD) is a favoured route for growing diamond films from gas mixtures comprising hydrogen and a small amount of a hydrocarbon precursor (typically methane).[1-4] Adding Ar to the CH_4/H_2 plasma has variously been reported to influence the film growth rate,[5,6] its surface morphology and the average crystallite size.[7-9] Synthesis of (ultra)nanocrystalline diamond films has even been reported from MW-activated gas mixtures involving just CH_4 and Ar as process gases.[10,11] Small additions of Ar have been used as an actinometer for estimating relative H atom concentrations in CH_4/H_2 plasmas.[12-15] Larger additions of Ar (and other noble gases) substantially affect the relative intensities of the various features in the optical emission spectrum of the plasma, as a result of changes in gas temperature and the plasma chemistry.[16-21]

Successful CVD of high-quality diamond depends on the availability of suitable concentrations of both H atoms and CH_x (x = 0-3) radicals, particularly CH_3 radicals, in the gas phase adjacent to the growing surface. H atom production is dominated by thermal dissociation of H_2 in the hot plasma region, so the benefits of replacing some H_2 in the process gas mixture by, for example, Ar might not be obvious. However, Ar is much heavier than H_2. Any substantial addition of Ar will thus reduce the thermal conductivity of the gas, and increase the gas temperature and the thermal dissociation of H_2 in the hot plasma core. Thus, as we demonstrate below, the H atom mole fraction (X(H)) may be maintained or even enhanced, notwithstanding the reduction in H_2 input mole fraction ($X_0(H_2)$) that accompanies an increase in the Ar input mole fraction, X_0(Ar).

We recently reported spatially and wavelength resolved optical emission imaging studies of MW-activated hydrogen plasmas operating with input powers, gas pressures, and gas and electron temperatures (T_g and T_e, respectively) relevant to contemporary diamond CVD reactors.[22] Complementary self-consistent two-dimensional (2-D) modeling of the various plasma-chemical, transport and electromagnetic processes allowed characterisation of the dominant plasma and plasma emission generation mechanisms, and served to highlight the importance of associative ionization and quenching reactions involving electronically excited hydrogen atoms (H*) and molecules (H_2*) with the alternate ground state species in establishing the observed emission intensities, I_{em}, their spatial distributions, and their sensitivity to process conditions.

Here we extend the use of spatially resolved optical emission imaging methods to explore the effects of progressive additions of noble gas R (Ar and, less extensively, Kr) to such H_2 plasmas. In addition to affecting T_g, the introduction of noble gas atoms opens new energy transfer pathways, including quenching of H* and H_2* emissions and the excitation and ionization of H and H_2 by collision with excited noble gas species – all of which processes can modify the (spatially dependent) electron energy distribution function (EEDF) of the plasma. These data illustrate the potential shortcomings of monitoring optical emission from a single location within such reactors. Emissions from the R atoms constitute another observable, and the variations in their emission intensities and spatial distributions upon changing process conditions offers another point of comparison with the self-consistent 2-D plasma modeling. Such comparisons provide a particularly clear illustration of the mass-dependent thermal diffusion prevailing in mixtures comprising light and heavy gas species and large temperature gradients and help to establish the relative importance of the various noble gas enabled plasma processes. Additionally, we note the observation of emissions from electronically excited Cu* atoms at high noble gas input mole fractions, X_0(R), and consider likely mechanisms by which such species are released into the gas phase from the reactor base plate.

2. Experimental

The CVD reactor, MW power supply, process gas regulation and optical emission imaging set-up have all been described previously.[22] H_2, Ar and Kr were all sourced from BOC (stated purities 6N, 5N and 5N, respectively) and used as supplied. These gas purities, plus the finite vacuum achievable in reactors of this type, mean that the process gas necessarily contains a few parts per million (ppm) of air – which is included in the later modeling. Base conditions for the present experiments were chosen as: total pressure p = 150 Torr and applied MW power P = 1.5 kW. The substrate (a 32 mm diameter, 3 mm thick, cylindrical disc of (generally) tungsten, though a molybdenum substrate was used for the measurements involving Kr additions) was mounted axi-symmetrically on a 0.01″ thick annular Mo spacer wire on a water-cooled oxygen-free electronic grade copper sample stage. Indicative substrate temperature (T_{sub}) values were obtained by one and/or two color optical pyrometry though, we recognise that near infrared emissions from H_2* species can distort such temperature measurements.[22] Gas mixing ratios were varied in either of two ways: (i) by matching any increase in the noble gas flow rate F(R) by a corresponding decrease in $F(H_2)$ such that the

total flow rate F_{total} = $F(H_2)$ + F(R) = 300 standard cm^3 per minute (sccm), and (ii) by increasing F(R) while holding $F(H_2)$ = 300 sccm and adjusting the pumping rate to maintain the required gas pressure. Given sufficient time for re-equilibration after any change in process conditions, the two methods demonstrate the same trends in emission intensities, I_{em}, their spatial distributions, and their sensitivity to X_0(R).

Emissions from the plasma were monitored using a Czerny-Turner spectrograph with a 50 mm focal length, f/16 objective lens. The H_2*, Ar* and Cu* emissions in the H_2/Ar plasma studies were dispersed using a 700 grooves mm^{-1} grating (a 400 grooves mm^{-1} grating was used for the H_α measurements and for all measurements involving H_2/Kr plasmas) and detected on a cooled CCD detector with an overall spatial magnification of ~0.08. These choices yielded resolutions of ≈0.04 nm/pixel and ≈0.06 nm/pixel (with the 700 and 400 grooves mm^{-1} gratings, respectively) at λ = 600 nm when using a 10 μm entrance slit, and a spatial (vertical) resolution of better than 0.5 mm. Each image was accumulated for (or scaled to an equivalent accumulation time of) 640 s. Given the small lens aperture employed, we assume that emission from the entire depth of the plasma is being sampled (*i.e*. that we are reporting column integrated line intensities).

3. Results and Discussion

As in our recent spatially resolved optical emission imaging studies of MW-activated hydrogen plasmas [22] it is appropriate to report the experimental observations and the plasma chemical modeling – both as functions of process conditions and location within the reactor – in sequence, and then conclude by summarising areas where experiment and model agree well, and areas where discrepancies remain. For conciseness, the narrative uses a considerable number of acronyms. Each is defined when it first appears but, to aid readers, these are also all collected in Table S1 of the Supporting Information (SI).

3.1 Experimental Results

Spatially resolved emission was imaged throughout the 250-950 nm wavelength range, under a range of operating conditions. The images report wavelength (λ) resolved column integrated emission intensities as a function of height (z) above the substrate surface. Analyses at fixed z return $I_{em}(\lambda)$ spectra, which allow identification of characteristic H_2*, H_α, Ar*, Kr* and Cu* emissions used in this work, which are detailed in Table 1. Illustrative images of H_2(d–a), H_α and Ar* emissions are shown in Figures S1 and S2 of the SI, while

Figure S3 shows the key excited states of H_2*, H*, Ar* and Kr* plotted on a common energy scale.

Vertical cuts through the images at the appropriate wavelength yield the spatial profile ($I_{em}(z)$) of the emission of interest. Figure 1 shows $I_{em}(z)$ plots for (a) the H_2* d–a (Fulcher band), v′=0–v″=0, Q(3) transition, (b) the H* (Balmer-α) transition and (c) and (d) the Ar* 696.54 and 811.5 nm emissions, as a function of X_0(Ar). For the data shown in Figures 1(a) and 1(b), $F(H_2)$ and P were held fixed at, respectively, 300 sccm and 1.5 kW, F(Ar) was progressively increased from 0 to 300 sccm and the pumping speed adjusted to maintain p = 150 Torr. Experiments using the same X_0(Ar) but maintaining F_{total} = 300 sccm returned the same spatial profiles and trends with changes in process conditions. The I_{em}(Ar*) profiles shown in Figures 1(c) and 1(d) were taken using this alternative strategy.

The H_2* emission profile for the pure H_2 plasma (*i.e.* X_0(Ar) = 0) shown in Figure 1(a) peaks at small z (~ 2 mm) and declines to near zero by z ~ 20 mm, as reported previously.[22] Increasing X_0(Ar) causes a decrease in $I_{em}(H_2*)$, most noticeably at larger z; the decline in $I_{em}(H_2*)$ is z dependent. The $I_{em}(H_2*)$ profile in the presence of Ar still peaks at small z, but the overall $I_{em}(H_2*)$ signal decreases faster than the decline in $X_0(H_2)$. $I_{em}(H_2*)$ profiles monitored via the G–B emission (Figure S4(a)) showed essentially identical trends with increasing X_0(Ar). The longer wavelength H_2* e–a emission reported in our recent studies of MW-activated H_2 plasmas [22] proved less useful when viewed in the presence of the (relatively much more intense) noble gas emissions.

The $I_{em}(H_\alpha)$ emission profile for the pure H_2 plasma operating at base conditions peaks at z ~7.5 mm, *i.e.* in the core region, and extends to z ~20 mm.[22] Upon introducing Ar, $I_{em}(H_\alpha)$ in the core region declines roughly proportionally with $X_0(H_2)$ but, as Figure 1(b) shows, a secondary maximum becomes increasingly evident nearer the substrate. Equivalent data for the H_β and H_γ transitions are also included in Figure S4. $I_{em}(H_\alpha)$ declines less steeply than $I_{em}(H_2*)$ with increasing X_0(Ar).

Figure 1(c) shows the spatial profiles of the Ar* emission at 696.54 nm recorded for different X_0(Ar) values. The displayed data in this case were obtained at a constant F_{total}; each increase in F(Ar) was compensated by a matching decrease in $F(H_2)$. As noted above, however, each of these spatial profiles was indistinguishable from that obtained by adding the appropriate F(Ar) to a constant $F(H_2)$ = 300 sccm and increasing the pumping speed to maintain p = 150

Torr. The X_0(Ar) dependent profiles of the I_{em}(Ar*) emissions at 811.53 and 826.45 nm are shown as Figure S5. Both are indistinguishable from those shown in Figure 1(c). This is noteworthy. As Table 1 shows, the 696.54 and 826.45 nm emissions share a common upper level (the $2p_2$ level in Paschen notation), but the former terminates on a metastable ($J = 2$) level arising from the ……$3p^5(^2P°_{3/2})4s^1$ configuration (the $1s_5$ level in Paschen notation). In principle, therefore, the former emission must be more susceptible to self-absorption, but the very similar X_0(Ar) dependences displayed by all three Ar* lines indicates that such effects are not important under the prevailing experimental conditions, even when X_0(Ar) = 0.5. Figure 1(d) shows an alternative presentation of the I_{em}(Ar, 811.53 nm) data in which each profile is scaled to a common maximum peak intensity. All peak at z ~2 mm and decline to zero by z ~20 mm but the profile is clearly X_0(Ar) dependent: the relative intensity at small z increases with increasing X_0(Ar).

The very different z dependent spatial and X_0(R) dependences of $I_{em}(H_2^*)$, $I_{em}(H_\alpha)$ and I_{em}(R*) are summarised in the I_{em}(z = 2 mm) and I_{em}(z = 7.5 mm) vs X_0(R) plots shown in Figure 2. This figure also serves to highlight that 'traditional' OES measurements that view just a localised region of such plasmas through an optical fibre could return very different $I_{em}(H_2^*)$, I_{em}(R*) and, particularly, $I_{em}(H_\alpha)$ vs. X_0(R) dependences simply according to the choice of z.

Figure 3 shows sample data from similar (albeit less extensive) studies of MW activated H_2/Kr plasmas. The changes in the profiles and intensities of the $I_{em}(H_2^*$, d–a) and $I_{em}(H_\alpha)$ emissions with increasing X_0(Kr) are broadly similar to those observed when increasing X_0(Ar) – as is also summarized in Figure 2. Equivalent $I_{em}(H_\gamma)$ versus X_0(Kr) data are shown in Figure S6. The variations in I_{em}(Kr*, 431.96 nm) with X_0(Kr) (Figure 3(c)) are very reminiscent of that observed with Ar. Similar data for the Kr* emissions at 427.40 and 437.61 nm are also included in Figure S6. The two shorter wavelength transitions terminate on a metastable level of Kr, whereas the 437.61 nm transition does not; again, the observed insensitivity to the choice of probe transition implies that self-absorption effects are not important under the prevailing experimental conditions.

As noted previously,[17] increasing the Ar or Kr fraction in the process gas reduces the thermal conductivity of the plasma and increases T_g in the core, and T_{sub}. The latter increase is evident by eye – the substrate becomes visibly red upon increasing the Ar (Kr) fraction – and by

pyrometry. These changes, which are detailed in Table S2, are paralleled by the appearance of additional features in the optical emission image which are attributable to electronically excited neutral copper atoms. Figure 4(a) shows spatial profiles of the 324.75 nm emission from Cu* atoms measured for different MW activated H_2/Ar mixtures operating under base conditions of p and P, at F_{total} = 300 sccm. Identical profiles were recorded for the (weaker) 327.40 nm emission feature. All peak at z ~ 2 mm and decline to zero by z ~ 16 mm. I_{em}(Cu*) increases rapidly with increasing X_0(Ar), as shown in Figures 4(b) and 4(c). The source of the copper must be the water-cooled base plate on which the W or Mo substrate sits. Discussion of likely mechanism(s) by which Cu enters the gas phase is reserved until section 3.3.3, pending consideration of the changes in H_2 plasma chemistry and composition induced by the progressive addition of noble gas.

3.2 Modeling the MW activated H_2/Ar plasma

The present study employed the self-consistent 2-D(r, z) model used in our recent studies of MW activated hydrogen plasmas,[22] where r and z are, respectively, the radial and axial distances from the center of the substrate surface as shown in Figure S7. This model, which contains specific blocks that address the plasma-chemical and electron kinetics, heat and species transfer, gas-surface interactions, and Maxwell's equations to calculate the MW electromagnetic fields, was tuned to capture the various effects of Ar additions on the transport processes, the plasma parameters and the plasma-chemical and electron (e) kinetics. This required re-calculation of the electron energy distribution functions (EEDFs) for all cells in the (r, z) grid, using sets of e-H, e-H_2, e-Ar, e-H_2O and e-ion collision cross-sections (for different gas mixture compositions, reduced electric fields and T_g) to provide the necessary rate coefficients for the plasma-chemical kinetics and the MW electromagnetic field blocks. Comparing the model outputs with the spatially resolved OES data recorded at different X_0(Ar) then allows investigation of the sources and sinks of the H*, H_2* and Ar* excited states and identification of the more important production and loss reactions for these species. Base conditions for the modeling were as close as possible to those used in the experimental study, *i.e.*, p = 150 Torr, P = 1.5 kW and Ar/H_2 gas mixtures with different X_0(Ar) in the range 0–0.4 and an air impurity in the range ~4–12 ppm. As in our recent studies of MW activated hydrogen plasmas, any O_2 impurity will be converted to H_2O molecules under the prevailing reactor conditions (*i.e.* high T_g and high H atom mole fraction, X(H)), which then activate the inter-conversion between H_3^+ and H_3O^+ ions.[22]

Four gas mixtures were explored to trace the effects of adding Ar to a hydrogen plasma and to compare with the spatially resolved OES measurements. The total pressure and MW power were held fixed (at p = 150 Torr P = 1.5 kW) in each of these simulations, but the mixtures were distinguished by the respective argon input mole fractions, X_0(Ar) = 0, 0.07, 0.33, and 0.4, and the associated level of air contamination (4.5, 5.7, 10.3 and 11.5 ppm). For completeness, a pure (*i.e.* zero air contamination) H_2/Ar mixture with X_0(Ar) = 0.33 but assuming otherwise identical process conditions was investigated also. The model outputs presented in this paper are all for the air-contaminated mixtures defined above. Outputs for the uncontaminated H_2/Ar mixture are reserved for the SI, but any significant differences caused by the air contamination are highlighted at the relevant points in the text. The substrate temperatures for these four X_0(Ar) regimes were calculated to be T_{sub} = 900, 925, 1080 and 1110 K, from a balance of plasma heating (by conductive heat transfer through the gas and H atom addition and abstraction reactions at the substrate surface) and cooling. Substrate cooling in the present reactor is by conductive heat transfer from the base of the substrate through the gas gap to the reactor base plate and is thus moderated by increasing the Ar fraction in the process gas mixture. The predicted increases in T_{sub} match experimental observation, though the absolute temperatures returned by the modeling are lower than those returned by optical pyrometry (as illustrated in Table S2). The most important effects of adding Ar to a hydrogen plasma are now described, with particular emphasis on the emitting gas phase species.

3.2.1 The effects of Ar addition on the electron energy distribution, MW power absorption and transport processes.

Any significant addition of Ar to a hydrogen plasma will change the plasma parameters and transport coefficients. For example, the thermal conductivity and diffusion coefficient of H atoms in a 25% Ar in H_2 mixture are, respectively, ~38% and ~20% smaller than in a pure hydrogen plasma.[23,24] The combined effects of thermodiffusion transfer [25] and the thermal dissociation of H_2 ensure that the Ar mole fraction X(Ar) in the hot plasma core (where T_g ~3000 K) is significantly less than in the input gas mixture. For example, X(Ar) in the plasma core is calculated to be ~0.25 for a 40% Ar in H_2 input mixture, and only ~0.035 in the core of the plasma from a 7% Ar in H_2 mixture. The rate coefficient for electron–Ar elastic collisions (k_{elas}(e-Ar)) is lower than k_{elas}(e-H_2) under the conditions prevailing in the plasma core, *e.g.* k_{elas}(e-Ar)/k_{elas}(e-H_2) ~0.3 and ~0.4 for 3.5%Ar/12%H/H_2 and 25%Ar/12%H/H_2

mixtures, respectively. The decrease in electron collision frequency upon Ar addition affects the absorption of MW power and the electromagnetic (E, H) fields and thus the EEDF, $f(\varepsilon)$. As shown in our recent hydrogen plasma studies,[22] the EEDF depends on the reduced electric field, $|E|/(N\times a)$, T_g, the population distribution in the rovibrational (v, J) levels of the ground (X) state H_2 molecules, the mole fractions of H(n = 1) atoms, X(H), and, additionally for the present study, X(Ar). Here $|E|$ is an absolute value of the electric field averaged over the MW period, N is the total gas concentration, and $a = (1+\omega^2/\nu^2)^{0.5}$, where $\omega = 2\pi f$ (with f = 2.45×10^9 s^{-1}) and ν are the MW and electron collision frequencies, respectively. The Boltzmann kinetic equations are solved numerically [22,26] in the different (r, z) cells for various plasma conditions and gas compositions of interest, and with proper inclusion of all important electron impact induced processes including excitation and de-excitation of population in the various rotational and vibrational levels of H_2.

As in an H_2 plasma,[22] the EEDFs in these H_2/Ar plasmas show two temperature components, with the general form $f(\varepsilon) = c_1\times\exp(-\varepsilon/T_1)$ for the energy range $2 \le \varepsilon \le 10.2$ eV and a high energy tail described by $f(\varepsilon) = c_2\times\exp(-\varepsilon/T_{tail})$ for $\varepsilon \ge 10.2$ eV and respective temperature T_{tail}. EEDFs were calculated for an array of $|E|/(N\times a)$, T_g, X(H) and X(Ar) values in order to determine process-dependent rate coefficients $k_i = \int v\sigma_i(\varepsilon)f(\varepsilon)d\varepsilon/\int f(\varepsilon)d\varepsilon$, where $v = (2\varepsilon/m_e)^{0.5}$ and m_e are the electron velocity and mass, respectively, and $\sigma_i(\varepsilon)$ is the (energy dependent) cross-section for process i. Figure 5 shows a selection of normalized EEDFs, $f(\varepsilon)/n_e$ (where $n_e = \int f(\varepsilon)d\varepsilon$ is the electron concentration), T_{tail} and average electron temperature T_e (*i.e.* effectively T_1) values for a constant reduced electric field ($|E|/(N\times a)$ ~33.4 Td) and H atom mole fraction (X(H) = 0.12) but different Ar mole fractions x in xAr/12%H/H_2 mixtures. The slope of the tail of the EEDF (T_{tail}) is essentially invariant: upon substituting (some) H_2 by Ar, electron impact excitation (EIE) and electron impact ionization (EII) of Ar atoms compensates for the EIE and EII of the replaced H_2. T_e increases upon replacing H_2 by Ar, however, because electron energy loss through rovibrational state changing collisions with H_2 is reduced.

Previous studies of the effect of higher Ar fractions in, for example, plasmas derived from ≥75%Ar/CH_4/H_2 input gas mixtures identified substantially higher T_e values.[18] For lower Ar dilutions (*e.g.* the ≤40%Ar/H_2 input gas mixtures modelled here), however, increasing X(Ar) at constant reduced electric field does not imply a similar change in T_e when comparing MW

activated H_2/Ar and H_2 plasmas. This is because, as Figure 6 shows, substituting Ar for some of the H_2 leads to a reduction in the reduced electric fields in the plasma core (by 10-15% upon increasing X_0(Ar) from 0.07 to 0.33), with the net result that T_e is little changed. This change in X_0(Ar) also leads to a ~30% reduction in the absorbed power density jE (averaged over the period of the MW field) in the plasma core. This decrease in jE is accommodated by a radial expansion of the plasma core (Figure 6(b)); the plasma size in the z direction barely changes (Figure 6(a)).

The radial expansion of the plasma core with increasing X_0(Ar) is also evident in the radial distributions of n_e, T_g and [H] shown in Figure 7(a), and from the axial column power density distributions shown in Figure S8 in the SI. We return to compare the data shown in Figure 7(a) with the corresponding n_e, T_g and [H] distributions at z = 0.5 mm (*i.e.* close above the substrate surface, Figure 7(b)) in section 3.3.1. The quantity plotted in Figure S8 – the calculated axial power density weighted by the area of the annulus associated with the cell at radius r, *i.e.* the quantity $2\pi r dr \times \int |jE(r,z)| dz$ with dr = 0.1 cm – clearly shifts to larger r with increasing X_0(Ar). Figure S8 also serves to illustrate another important conclusion relating to the 'size' of the plasma volume. One (visible) measure would be the radial extent of the glowing plasma region which, in the present context, is reasonably modelled as the volume within which the concentrations of emitting species are within an order of magnitude of their maximal values. The horizontal bars in Figure 7(a) illustrate the radial extents of the H_2/Ar plasma volumes with X_0(Ar) = 0, 0.07 and 0.33 according to this definition, using the excited state concentrations shown in Figure 8. However, as Figure S8 also shows, ~30-35% of the input power in these H_2 and H_2/Ar plasmas is absorbed outside this region, *i.e.* in a large, 'cool' (T_e < 1 eV) peripheral volume where n_e is still in the range ~10^9-10^{11} cm^{-3} (Figure 8). Proper recognition of this electron concentration in the 'cool' plasma is important for any correct partitioning of the absorbed power in the 'hot' and 'cool' plasma regions.

3.2.2 H_2/Ar plasma-chemical kinetics, including the effects of inter-conversion between ions and air contamination.

Kinetic schemes involving charged species and excited states of atomic hydrogen (H*), molecular hydrogen (H_2*) and argon (Ar*) were developed on the basis of previous experimental and theoretical studies.[17,18,26-34] Table 2 lists the most important reactions involving excited and charged species, along with the associated rates and rate coefficients. A

longer list of the more important reactions (with parameterized reactions and rate coefficients used in the present modeling and a longer reaction list (with parameterized rate coefficients and details of the data sources) can be found in Table S3. The H(n = 6) state (with an excitation energy of 13.22 eV) is included simply to illustrate the possible effects of near resonant energy transfer with Ar($3p^5 4p$) states ($2p_i$ states in Paschen notation, with excitation energies in the range 12.9-13.5 eV for i = 1-10), henceforth denoted simply as Ar(4p). Our recently reported H_2 plasma kinetics scheme [22] was used with minor modifications, *e.g.* use of $H_2(a^3\Sigma_g^+)$ instead of $H_2(B^1\Sigma_u^+)$ in the H(n = 1) + H_2* $\rightarrow$ H(n = 3) + H_2(X) coupling reaction, thermochemical data for the important ions H_3^+, H_3O^+ and ArH^+ from ref. 35 and experimental cross-sections for the respective electron–ion recombination reactions.[36-38]

A. Charged Species: We start by considering the balances between the various charged species and the charged species distributions and how these influence the plasma chemistry. The electron and ion concentrations in the hot plasma core are determined by the balance of the main sources (EII (reactions (20)-(22) in Table 2) and associative ionization (reactions (23) and (24)) and sinks (ambipolar diffusive transfer to the substrate and out of the plasma core, and dissociative recombination (DR) of molecular ions with electrons (reactions (17)-(19))). As Table 2 shows, ionization of argon is minor compared to hydrogen (H and H_2) ionization and, as in the pure hydrogen plasma,[22] the associative ionization reaction H(n = 2) + $H_2 \rightarrow H_3^+$ + e dominates. The electron and ion concentrations in the 'cool' plasma regions, in contrast, are determined by the balance between the main sources (ambipolar diffusion of charged species from the plasma core) and sinks (DR processes). The rate coefficients k_{DR} for dissociative recombination over the wide range of plasma conditions (*e.g.* their variation with T_e and T_g) relevant to the present study remain a subject of controversy.[36-39] At low gas temperatures (*e.g.* room temperature) k_{DR} is inversely proportional to T_e^{b0} (*i.e.* $k_{DR}=k0_{DR}/T_e^{b0}$) with exponent b0 ~ 0.5-0.7.[39] Higher values (b0 ~ 1-2) have been suggested at higher T_g (*e.g.* at T_g >1000 K) [39] and it has also been suggested that k_{DR} may be sensitive to T_g (*e.g.* $k_{DR} = k0_{DR}/(T_e^{0.5}T_g)$).[40] Both alternatives were probed in our previous study [22] and $k0_{DR}$ varied so as to achieve the best match with the measured I_{em} profiles – encouraging use of the T_g dependent function in the systematic calculations. Now we have calculated k_{DR} directly using the literature DR cross-sections (see Table S3) and the appropriate local EEDF resulting in $k_{DR} \sim k0_{DR}/T_e^{b0}$ dependence with b0 ~0.5. In addition, we explored the T_g dependence of the rate coefficient for DR assuming a $\sim 1/T_g^{b1}$ functional form while conserving the same

optimal k_{DR} values in the plasma core. The value b1 = 0 (*i.e.* assuming no T_g dependent reduction of the DR coefficient) was found to provide a slightly better correlation with the measured I_{em} profiles. As Table 2 shows, this analysis reveals rate coefficients $k_{DR}(ArH^+) << k_{DR}(H_3^+) < k_{DR}(H_3O^+)$ (reactions (17)-(19)) under the process conditions of interest and a total DR rate that is very sensitive to the local concentrations of the respective ions. For completeness, we note that Table 2 allows an ambiguity regarding the products of reactions (17) and (18), since neither is a significant source of any of the suggested products. DR involving H_2^+ ions is not listed in Table 2 as the maximal calculated $[H_2^+]$ in the hot core region is three orders of magnitude lower than that of $[H_3^+]$.

Redistribution between the dominant ions is driven by fast ion interconversion reactions (*e.g.* (43) and (44)), that depend on the respective neutral species concentrations and T_g (the ion temperature T_i is close to T_g at the prevailing pressures and reduced electric fields). Ar^+ ions formed by EII (reaction (22)) are converted efficiently to ArH^+ ions via the exothermic reaction $Ar^+ + H_2 \leftrightarrow ArH^+ + H$, thus ensuring that $[ArH^+] >> [Ar^+]$. However, the ArH^+ concentration is determined by the balance of the fast forward (exothermic, with reaction enthalpy $\Delta H_{43} \sim -0.55 \pm 0.05$ eV) and reverse (endothermic) reactions $ArH^+ + H_2 \leftrightarrow H_3^+ + Ar$ (reactions (43) and (–43), respectively).[41] These reactions are in local equilibrium throughout the whole reactor ensuring $[ArH^+] \approx k_{-43}[H_3^+][Ar]/(k_{43}[H_2])$. The forward reaction rate coefficient is reasonably well defined ($k_{43} = 6.3\times10^{-10}$ (ref. 30), 8×10^{-10} cm^3 s^{-1} (ref. 41)) but k_{-43} has been controversial [30] and its determination in the current context is complicated by the need for $k_{-43}(T_g)$ values over a wide range of temperatures (from ~300 to ~3000 K). $k_{-43}(T_g)$ was estimated from the temperature dependent heat capacities, entropies and enthalpies of Ar, H_2, ArH^+ and H_3^+ (ref. 35) and found to be a rapidly rising function of T_g that is reasonably approximated in Arrhenius form: $k_{-43}(T_g)$ / cm^3 s^{-1} $\approx 6.5\times10^{-9}\times\exp(-6830/T_g)$; yielding $k_{-43}(T_g = 300\text{ K}) \approx 10^{-18}$ cm^3 s^{-1} and $k_{-43}(T_g = 2700\text{ K}) \approx 5\times10^{-10}$ cm^3 s^{-1}. This analysis provides the relationships $[ArH^+] \approx [H_3^+]\times[Ar]/[H_2]$ in the hot plasma core (*i.e.* at $T_g \sim 3000$ K) and $[ArH^+] < 2\times10^{-3}\times[H_3^+]\times[Ar]/[H_2]$ in peripheral regions of the reactor (with $T_g < 800$ K). We return to discuss this latter relationship in the context of the observed Cu* emissions in section 3.3.3.

An analogous relationship between H_3O^+ and H_3^+ ions ($[H_3O^+] \approx k_{44}[H_3^+][H_2O]/(k_{-44}[H_2])$) is valid in hot regions only, *i.e.* where $T_g > 2500$ K and the forward exothermic (44) and reverse

endothermic (−44) reactions are in approximate balance. Given the high endothermicity of reaction (−44) (ΔH_{-44} ~2.74±0.04 eV), the k_{-44} coefficient calculated from the available thermochemical data becomes too low in cold regions where H_3O^+ ions accumulate and start to dominate the ion distribution. This coefficient can also be approximated in Arrhenius form: $k_{-44}(T_g)$ / cm^3 s^{-1} ≈ $2.3\times10^{-12}\times T_g\times\exp(-29300/T_g)$. In contrast to reactions (43) and (44), the role of reactions 45 and (−45) (with deduced rate coefficient $k_{-45}(T_g)$ ≈ $7.4\times10^{-14}\times T_g^{1.4}\times\exp(-34500/T_g)$ and reaction enthalpy ΔH_{-45} ~ 3.3±0.1 eV) in facilitating interconversion between the various ions is negligible under the prevailing conditions (Table 2). The radial (at z = 10.5 mm) and axial (at r = 0) profiles of the electron concentration is not explicitly shown in Figures 8 and 9 but can be obtained as $n_e \approx \{[H_3^+] + [H_3O^+] + [ArH^+]\}$. Again, the selective radial expansion of the plasma upon increasing the Ar content (discussed in section 3.2.1) is evident from comparing the r (and z) profiles of the total ion concentration shown in Figures 8 (and 9) and, more clearly, by viewing the same total ion (or the n_e) density profiles plotted on a linear scale (Figure S10).

Plots analogous to those shown in Figs. 8(b) and 9(b) for a H_2/Ar plasma with X_0(Ar) = 0.33 and zero air contamination are shown in Figure S9. Comparing these data shows that the assumed air contamination has minimal effect on n_e or its spatial dependence but substitutes the H_3^+ (and ArH^+) ions at the periphery of the plasma by H_3O^+ ions and causes a modest (<10-20%) change in the concentrations of H(n=3) and other excited species in the plasma core.

B. Electronically Excited Species: The modeling returns the following picture of the balances and couplings involving electronically excited species. We identify three reservoirs of excited species (H*, H_2* and Ar*, with respective excitation energies $E_H \geq$10.2, $E_{H2} \geq$11.3 and $E_{Ar} \geq$11.57 eV). The primary pumping mechanism for each of these reservoirs is EIE of the corresponding ground state species, *i.e.* H(n = 1), H_2 and Ar. In what follows, we analyze the local balance of excited state production and loss reactions in the region of maximal EIE rates (*i.e.* at z ~3.5 mm and r = 0). Key parameters for this region of an H_2/Ar plasma with X_0(Ar) = 0.33 and base p (150 Torr) and P (1.5 kW) are: T_g = 2713 K, $|E|/(N\times a)$ = 34 Td, X(Ar) = 0.188 and X(H) = 0.083. The present modeling returns the following total EIE rates: R_{EIE}(H) ~6×10^{16} cm^{-3} s^{-1}, $R_{EIE}(H_2)$ ~1.83×10^{17} cm^{-3} s^{-1} and R_{EIE}(Ar) ~1.2×10^{16} cm^{-3} s^{-1} (Figure 10). Contributions from the many higher excited states neglected in the modeling will

ensure that each of these values slightly underestimates the total EIE rates. We also note that the H_2 dissociation rate in the plasma region following EIE to the unstable $H_2(b^3\Sigma_u^+)$ state (reaction (6) in Table 2), $R_{EID}(H_2) = 2.44\times10^{18}$ cm^{-3} s^{-1}, far exceeds the sum of all other EIE rates and thus treat this electron impact dissociation (EID) as a separate (and important) pathway. As shown in Table 2 and Figure 10, the EII rates R_{EII}(H, H_2 and Ar) are 2-3 orders of magnitude lower than R_{EIE}.

The total excitation rate (*i.e.* the sum of all R_{EIE} values) is balanced by the rates of:
(i) reactive quenching (R_{RQ}) and radiative decay (R_{rad}) of the H*, H_2* and Ar* excited states, including the following major loss contributions (Table 2): $R_{RQ}(H_2^* + H_2 \rightarrow 2H + H_2) \sim10^{17}$ cm^{-3} s^{-1}, $R_{RQ}(H(n = 2) + H_2 \rightarrow 3H) \sim6.1\times10^{16}$ cm^{-3} s^{-1}, $R_{RQ}(Ar^* + H_2 \rightarrow 2H + Ar) \sim1.1\times10^{16}$ cm^{-3} s^{-1}, $R_{rad}(H_2(B^1\Sigma_u^+ \rightarrow X^1\Sigma_g^+) + h\nu) \sim4.2\times10^{16}$ cm^{-3} s^{-1}, $R_{rad}(H_2(a^3\Sigma_g^+ \rightarrow b^3\Sigma_u^+) + h\nu) \sim4.3\times10^{16}$ cm^{-3} s^{-1}, and
(ii) excitation transfer (R_{ET}) between these reservoirs (reactions (25)-(34) in Table 2).

These rates illustrate the transformation of electronic excitation energy and the balances between the various excited state production and loss mechanisms. About 72% of the total electronic excitation (*i.e.* the sum of all R_{EIE} rates for the three reservoirs apart from the (major) contribution associated with EID of H_2 in the plasma (reaction (6))) is expended on H_2, with ~23% used in exciting H atoms and only ~5% on exciting Ar atoms. Most (~66%) of this total excitation is balanced by reactive quenching (reactions (39)-(42)), leading to H_2 dissociation. The remainder is accommodated radiatively, with dominant contributions from $H_2(B^1\Sigma_u^+)$ and $H_2(a^3\Sigma_g^+)$ emission (reactions (36) and (37)). Including the full diversity of possible excitation transfer pathways in any model of H_2/Ar plasmas would be a huge challenge. Fortunately, the energy transfer rates (R_{ET}) between the H*, H_2* and Ar* excited states are much lower than their production rates (by EIE), and any model-dependent variations of these exchange rates would have only limited impact on the spatial profiles of the excited state column densities.

At this point it is worth re-emphasizing that only a very minor part of the absorbed MW power is utilized in the EIE processes probed by OES experiments. Even in the region of maximal EIE rates (Table 2 and Figure 10), the power density going into excited species (~0.5 W cm^{-3}) is only ~1% of the total absorbed power density (51 W cm^{-3}). The vast majority of the MW energy absorbed by the electrons is expended on gas heating – indirectly

(via vibrational and rotational excitation of H_2 molecules followed by vibrational-translational (V-T) and rotational - translational (R-T) relaxation of $H_2(v, J)$ on H atoms), and directly via the elastic collision of electrons with heavy particles.[17,18,26] [Note that the last column in Table 3 in ref. 17 contains a typographical error: The 70.2 entry should read 7.02].

Table 2 provides more details regarding the distribution of excitation rates within each reservoir and shows that the dominant (typically >90%) R_{EIE} contributions are to the lower excited states of each species, *i.e.* to H(n = 2), $H_2(B^1\Sigma_u^+)$, $H_2(a^3\Sigma_g^+)$, $H_2(c^3\Pi_u)$, $Ar(1s_{3,5})$ and $Ar(1s_{2,4})$. A more detailed description of the balance of production and loss reactions for separate H* and H_2* states was presented in the recent study of MW activated hydrogen plasmas.[22] Similar balances are observed for the Ar* states. For example, the local balance of the emitting Ar(4p) states explicitly included in this study is largely determined by EIE of ground state Ar atoms (R_{EIE} ~1.4×10^{15} cm^{-3} s^{-1}) and loss via both radiative decay (R_{rad} ~1.1×10^{15} cm^{-3} s^{-1}) and excitation transfer reactions with H(n = 1) and H_2. As found also for H and H_2,[22] EIE of excited state Ar atoms is unimportant (*cf.* EIE of ground state Ar atoms); the concentrations of Ar* species (even in the lowest metastable states) are just too low. The present modeling returns [Ar*]/[Ar] ratios <10^{-8} under the prevailing plasma conditions.

The local production and loss rates of the excited state species are in strong balance and the radial and axial concentration profiles shown in Figures 8 and 9 for H_2/Ar plasmas with X_0(Ar) = 0.07 and 0.33 are closely related to the spatial profiles of the sources and the quenching rates of the respective species.

3.3 Comparing the model outputs with experimental I_{em}(z) profiles

3.3.1 H*, H_2* and Ar* emissions

The H and H_2 plasma kinetics scheme described in ref. 22, supplemented with the additional H*/H_2*/Ar* reactions (including the more important reactions summarized in Tables 2 and S3), was used to simulate the various X_0(Ar) dependences identified experimentally. As Figures 11(a) and 11(b) show, the 2-D modeling succeeds in capturing the roughly proportional decline in $I_{em}(H_\alpha)$ and the greater than linear decrease in $I_{em}(H_2^*)$ observed with increasing X_0(Ar) (*i.e.* with decreasing $X_0(H_2)$). The measured I_{em}(Ar*, 696.54 nm) intensity grows near linearly with X_0(Ar). The I_{em}(Ar*, 696.54 nm; z) profile is determined by {$Ar(2p_2)$}, the column density of the emitting state. The present modeling assumes that

{Ar($2p_2$)} behaves in a similar manner to the total column density associated with all ten $2p_i$ states derived from the $3p^5 4p$ configuration, *i.e.* to {Ar(4p)}, given the likely strong mixing of the different $2p_i$ states through collisions with $H_2(v, J)$ molecules. Test calculations involving just the Ar($2p_2$) state, with its individual EIE cross-section rather than a total cross-section for the Ar + e $\rightarrow$ Ar(4p) + e process,[32] show some differences in the relative {Ar($2p_2$)} and {Ar(4p)} profiles – reflecting differences in the respective rates of EIE, ET, radiative and reactive quenching. Given the number of possible, but as yet only poorly characterised, ET, quenching and mixing processes for the various Ar($2p_i$) states, [27] we simply note the good qualitative correlations between the calculated column densities {Ar(4p)}(z) and measured I_{em}(Ar*, z) profiles at the various X_0(Ar) (Figure 11(c)). Arguably the most serious discrepancy between the modeling and observation is the much smaller predicted increase in {Ar(4p)} at low z at high X_0(Ar).

Similar shortcomings limit the extent to which the modeling replicates the measured $I_{em}(H_\alpha)$ and $I_{em}(H_2^*)$ profiles at different X_0(Ar). Figures 11(a) and 11(b), for example, show that the model returns relatively greater declines in {H(n = 3)} and {$H_2(d^3\Pi_u)$} at X_0(Ar) $\geq$ 0.33 than the observed reductions in $I_{em}(H_\alpha)$ and $I_{em}(H_2$(d-a)). An overestimation of the contributions from excitation transfer (ET) processes (27) and (28) in the case of H(n = 3) atoms and an underestimation of contributions from ET processes in the case of $H_2(d^3\Pi_u)$ (for which the current modeling includes no allowance for any coupling with high lying, near resonant states of Ar) may be responsible for these discrepancies. One indirect hint in support of this suggestion is provided by the calculated behaviour of {$H_2(e^3\Sigma_u^+)$}, for which the ET process (34) has a net positive effect: the predicted {H_2(e); X_0(Ar) = 0.4}/{H_2(e); X_0(Ar) = 0)} ratio is about twice the {H_2(d); X_0(Ar) = 0.4}/{H_2(d); X_0(Ar) = 0} ratio. Figure 11 also shows that the 2-D modeling fails to correctly describe the observed $I_{em}(z)$ profiles at small z.

The modeling succeeds in reproducing many of the trends observed when replacing a progressively greater H_2 fraction by Ar, including the spatially non-uniform decrease of $I_{em}(H_\alpha)$ and $I_{em}(H_2^*)$, the shift in the centre of gravity of the $I_{em}(H_\alpha)$ and $I_{em}(H_2^*)$ distributions to smaller z and the comparative insensitivity of the peak of the I_{em}(Ar*, z) distribution to changes in X_0(Ar). Several of the points of disagreement between the present observations and model outputs were also noted in our study of hydrogen plasmas,[22] and several possible contributory factors were proposed. For example, the modeling neglects non-local effects like diffusive transfer of electron energy and electron conduction, and any

imbalance in the ionization and electron-ion recombination rates is accommodated by the diffusional transfer of charged species to the substrate and the adjacent walls of the reactor. In the present context, we also note the limited number of species included in Table 2, and the fact that their associated kinetic schemes are far from complete.

The plasma emission is brighter at the periphery of the substrate (most notably at higher X_0(Ar)). This indicates a local maximum in the EM field that is confirmed by the present 2-D modeling, which predicts a more than order of magnitude increase in the charged species density near the substrate edge. By way of illustration, Figure 7(b) showed the electron concentration profile $n_e(r, z = 0.5$ mm) for H_2/Ar mixtures with X_0(Ar) = 0.07 and 0.33. However, the magnitudes of the predicted increases are not sufficient to reproduce the observed increase in the line-of-sight emission intensities at small z. The modeling also reveals another possible source of near edge emission – the formation of excited species in electron-ion dissociative recombination reactions (*e.g.* OH* products from reaction (18)), but the wavelength selective nature of the present experiments means that such emissions cannot contribute to the $I_{em}(z)$ intensities and profiles reported here.

The calculated radial profiles of [H] and T_g just above the substrate surface (at z = 0.5 mm) shown in Figure 7(b) for H_2/Ar plasmas with X_0(Ar) = 0, 0.07 and 0.33 highlight the way Ar additions reduce the radial variations of both quantities. For example, the predicted radial variations in the near substrate H atom density, $[H]_{ns}$, and the near substrate gas temperature, T_{ns}, are effectively halved upon increasing X_0(Ar) from 0 to 0.33, yet the absolute $[H]_{ns}$ density is barely compromised (because of the associated increase in the absolute value of T_{ns}). This 'smoothing' of the radial variations in $[H]_{ns}$ and T_{ns} are a consequence of the plasma expansion that accompanies Ar addition (recall section 3.2.1). Our recent H_2 plasma studies showed that increasing the MW power offered one means of enhancing the uniformity at the gas-substrate interface (reflecting the plasma volume $V_p \sim P$ dependence).[22] The present work suggests that strategic Ar additions could offer similar benefits with regard to achieving more uniform processing of the substrate area, *e.g.* more uniform rates of diamond CVD in optimized CH_4/H_2/Ar mixtures, as illustrated in recent growth studies at similar process pressures (p ~150 Torr) by Yamada *et al.*[21]

3.3.2. H_2/Kr plasmas

H_2/Kr plasmas have not been investigated so extensively – experimentally or theoretically – and here we concentrate on highlighting differences between H_2/Kr and H_2/Ar plasmas that derive from the properties of the two noble gases. Kr has a higher atomic mass (M_{Kr} = 83.8 u, *cf.* M_{Ar} = 39.9 u), a lower ionization potential (IP_{Kr} = 14 eV, *cf.* IP_{Ar} = 15.76 eV), a lower energy first excited state (E_{Kr} = 9.9 eV, *cf.* E_{Ar} =11.55 eV) and a lower thermal conductivity (λ_{Kr} = 0.09 mW cm^{-1} K^{-1}, *cf.* λ_{Ar} = 0.17 mW cm^{-1} K^{-1} at 1 atm and 0 ºC). These differences should ensure that, for any given X_0(R), the H_2/Kr plasma will be hotter and will involve a greater noble gas contribution to the total ionization. The former prediction is confirmed by substrate temperature measurements: the present study finds a greater relative increase in T_{sub} for a given X_0(R) when R = Kr, as did a previous comparative study of Ar- and Kr-rich methane/hydrogen plasmas (X_0(R) >0.93) for growth of ultrananocrystalline diamond (UNCD).[17] Even for these Ar- and Kr-rich plasmas, however, the process parameters for convenient UNCD deposition, the deposition rates and the crystallite sizes were rather similar, though the measured H(n = 2) and H(n = 3) column densities were an order of magnitude lower in the Kr-rich plasma.[17] This difference reflects efficient quenching in the near resonant reactions H(n = 2) + Kr → H(n = 1) + Kr($4p^5 5s^1$) and H(n = 3) + Kr → H(n = 1) + Kr($4p^5 5p^1$) for which – because of its different energy level structure – there are no analogues when R = Ar.[17]

Such differences are of less importance in the H_2-rich plasmas featured in the present study, wherein the dominant reactions of H(n = 2, 3) atoms are with H_2 molecules (reactions (25) and (41)) rather than R atoms. Thus the important associative ionization reaction (23) and thus the reduced electric field, T_e and the other plasma parameters will all vary reasonably smoothly and coherently upon adding either Ar or Kr to the present H_2-rich plasma. The plasma core remains H_2-rich, even for the highest X_0(R) (~0.5-0.66)) because of the thermodiffusive transfer of heavy species from the hot plasma core. The most striking differences in the present experimental findings for the H_2/Ar and H_2/Kr plasmas are the more pronounced reductions of $I_{em}(H_2^*)$ and $I_{em}(H^*)$ (Figure 2) and the relatively greater Cu* emissions (see Section 3.3.3) upon any given X_0(R) addition when R = Kr. Both observations can be traced to differences in the ionic component within the plasma. Namely, the fraction of KrH^+ ions ($[KrH^+]/n_e$) in the total distribution of ions should be much higher (especially in the cooler regions) than the ArH^+ fraction ($[ArH^+]/n_e$) due to the more favorable thermochemistry of KrH^+ formation and the respective ionization potentials of Kr and Ar. Kr has a higher proton affinity (PA_{Kr} = 4.41 eV, *cf.* PA_{Ar} = 3.85 eV) and a lower enthalpy for

forming KrH^+ ($\Delta H_{298}(KrH^+)$ = 11.5 eV, *cf.* $\Delta H_{298}(ArH^+)$ = 12.1 eV). As a result, the key charge transfer reaction

$$H_3^+ + Kr \leftrightarrow KrH^+ + H_2 \quad (46)$$

is almost thermoneutral ($\Delta H_{46} \sim 0$, *cf.* $\Delta H_{43} \sim -0.55$ eV) and the equilibrium is shifted in favor of the products: $k_{46}/k_{-46} \approx 15$ and $k_{46} > 10^{-10}$ cm^3 s^{-1} (ref. 42) and thus supports much higher $[KrH^+]/[H_3^+]$ (*cf.* $[ArH^+]/[H_3^+]$) ratios, especially in the cooler regions (including near the reactor base plate). Two further factors merit note. The higher $[KrH^+]$ concentration (>>$[ArH^+]$), and the concomitant reduction in $[H_3^+]$, should be expected to result in a lower total rate of DR in the H_2/Kr plasma. The higher ionization rate of Kr (*cf.* Ar, reflecting the lower IP of the former) will lead to a higher total ionization rate in a H_2/Kr plasma. Both these factors will act to decrease the reduced electric field $|E|/(N \times a)$ and T_e values in a H_2/Kr plasma in order to accommodate similar absorbed powers and n_e values in both plasmas at any given X_0(R). Such expectations are supported by test 2-D model calculations involving KrH^+ ions for X_0(Kr) = 0.07 and 0.33: T_e drops by ~10% and the rates of EII of Kr increase by roughly an order of magnitude, resulting in a faster decline of H* and H_2* with Kr addition (*cf.* an equivalent Ar addition) – in accord with the OES measurements (Figure 2).

3.3.3 Cu* emissions

The following description is largely focused on H_2/Ar plasmas but, as shown in section 3.3.2, similar (more advanced) effects operate in the case of H_2/Kr plasmas also. The base plate on which the substrate sits is the only source of copper in the proximity of the hot plasma. The observed Cu* emissions peak at low *z* and are observed only at higher Ar (and Kr) mole fractions (*e.g.* at X_0(Ar) >30%, Figure 4). These observations hint at sputtering (etching) of the Cu base plate by low energy heavy ions (*e.g.* ArH^+) and may have some parallels with previous studies demonstrating that an incident flux of H atoms substantially increases the Ar^+-ion induced sputter yield (and reduced the threshold sputtering energies) of a-C:H films.[43] We suggest that a similar synergetic interaction of radicals (H atoms), vacuum ultraviolet radiation from the distant H_2/Ar plasma core [44] and low energy ArH^+ ions with the Cu base plate is a likely source of the volatile Cu atoms observed in the present experiments. Figure 4(b) showed the I_{em}(Cu*) signal increasing steeply with increasing X_0(Ar). Comparison with the calculated ion concentrations adjacent to the base plate (Figure 4(c)) reveals an obvious correlation between I_{em}(Cu*) and the local ArH^+ concentration, but no

correlation with the (much higher) local concentrations of H_3O^+ and H_3^+ ions. We also note the possibility of producing CuH species (as a volatile product at the Cu surface) in the process of Cu–Cu bond breaking in the interaction with ArH^+, *i.e.* in e-ArH^+ DR at the Cu surface. Any such volatile CuH species would be readily destroyed at the high prevailing H atom concentrations. The CuH + H ↔ Cu + H_2 reaction is exothermic for forming Cu products in both the ground ($^2S_{1/2}$) or first excited ($^2D_{5/2}$) state. Quenching of any excited state Cu species will be efficient at the prevailing pressures, so the most abundant copper species diffusing away from the base plate will surely be Cu($^2S_{1/2}$) atoms, and EIE provides a ready route to populating the observed emitting Cu($^2P_{3/2}$) and Cu($^2P_{1/2}$) states (with respective excitation energies of 3.82 eV and 3.79 eV).

The local I_{em}(Cu*) signals at 324.75 and 327.4 nm are determined by the product of the EIE rate coefficient k_{EIE}, the electron density, n_e, and the concentration of ground state Cu atoms, [Cu($^2S_{1/2}$)]. [Cu($^2S_{1/2}$)] will be maximal just above the substrate as a result of its proximity to the source region (the base plate at z = –3 mm) and, as with Ar, as a result of thermodiffusive transfer driven by the drop in T_g at small z. The n_e term shows the opposite behavior at small z (see Figure 9, recognizing that $n_e \approx [H_3O^+] + [H_3^+] + [ArH^+]$). The observed maximum of I_{em}(Cu*), at z ~2-3 mm (Figure 4(a)), reflects the maximum of the product $k_{EIE}n_e$[Cu($^2S_{1/2}$)] and, in particular, the maximum of the calculated T_e distribution (Figure 6(b)). The calculated maximal concentrations of [ArH^+] above the Cu base plate are localized in the annulus immediately outside the substrate (*i.e.* in the region R_{sub}+1.5 < r < R_{sub}+4 mm, recall Figure 7(b)), and it is here that maximal sputtering rates should be observed. That I_{em}(Cu*) at any given X_0(R) is greater when R = Kr follows naturally from the greater relative KrH^+ concentrations (recall section 3.3.2). The Cu atoms in the gas phase above the base plate can be expected to reach their steady state concentrations within a short time after plasma ignition (a few seconds at most), with the flux of Cu atoms into the gas phase (from sputtering) compensated by loss as a result of diffusive expansion and redeposition onto proximal surfaces (the base plate and/or the substrate).

4 Conclusions

This combined experimental and modeling study explores ways in which MW-activated hydrogen plasmas operating under conditions relevant to contemporary diamond CVD

reactors, *i.e*. at a high gas temperature (T_g ~3000 K) and moderate pressure (p ~150 Torr), are affected by additions of noble gas (R = Ar and Kr). The experiments provided spatially resolved optical emission spectra from the d and G excited states of H_2, from the n = 3 level of atomic hydrogen and from various excited states of Ar and Kr, as functions of gas mixing ratio. The experimental data are compared and contrasted with the outputs of a self-consistent 2-D (r, z) model of the plasma-chemical, transport and electromagnetic processes prevailing in H_2/Ar plasmas with different X_0(Ar). Such comparisons allow characterization of the dominant plasma (and plasma emission) generation mechanisms prevailing in MW-activated H_2/Ar plasmas, and identification of the more important Ar–H, Ar–H_2 and H–H_2 coupling reactions. Noble gas addition causes a radial expansion of the plasma, and thus leads to more uniform [H] and T_g profiles just above the substrate – a finding that should find use when planning diamond growth experiments involving larger area substrates and dilute C/H/(Ar) gas mixtures. Noble gas addition in the current experiments is also found to exacerbate (unwanted) sputtering of the copper section within the reactor base plate. The observed gas phase Cu* emission intensities correlate well with the calculated ArH^+ (and KrH^+) ion concentrations just above the substrate surface but appear insensitive to the (relatively more abundant) H_3^+ and H_3O^+ ion concentrations in this region.

Additional Content

The following Supporting Information is available free of charge on the ACS Publications website at DOI:

Selected $I_{em}(\lambda, z)$ images of H_2(d–a), H_α and Ar* emissions from MW activated H_2/Ar plasmas; plot showing key excited states of H_2*, H*, Ar* and Kr* on a common energy scale; $I_{em}(H_2^*$, G–B), $I_{em}(H_\beta)$, $I_{em}(H_\gamma)$, I_{em}(Ar*, 811.53 nm) and I_{em}(Ar*, 826.45 nm) emission profiles as functions of X_0(Ar); $I_{em}(H_\gamma)$, I_{em}(Kr*, 427.40 nm) and I_{em}(Kr*, 437.61 nm) emission profiles from MW activated H_2/Kr plasmas as functions of X_0(Kr); radial distributions of the calculated axial column power density weighted by the area of the annulus associated with cells at radius r for H_2/Ar plasmas with X_0(Ar) = 0, 0.07, 0.33 and 0.4, p = 150 Torr and P = 1.5 kW; axial (at r = 0) and radial (at z = 10.5 mm) concentration profiles for selected species in H_2/Ar plasmas with X_0(Ar) = 0.33, zero air contamination, p =

150 Torr and P = 1.5 kW; axial (at r = 0) and radial (at z = 10.5 mm) concentration profiles of the total ion concentration in H_2/Ar plasmas with X_0(Ar) = 0.07 and 0.33, with p = 150 Torr and P = 1.5 kW, plotted on a linear scale to highlight the radial expansion and the minimal change in the axial dimension of the plasma volume upon increasing X_0(Ar).

Author Information

Corresponding Authors

*E-mail: mike.ashfold@bristol.ac.uk; ymankelevich@mics.msu.su

Notes

The authors declare no competing financial interests.

All underlying experimental data are available at the University of Bristol data repository, data.bris, at DOI: 10.5523/bris.81gdmets9gr22umh81j0gmxlb

Acknowledgements

The Bristol authors are grateful for financial support from the Engineering and Physical Sciences Research Council (EPSRC) through grant no. EP/K018388/1, the EPSRC Centre for Doctoral Training in Diamond Science and Technology (EP/L015315/1) and Element Six Ltd. The authors are also grateful for the many and varied contributions from Dr James Smith. The work was performed within the Cooperation in Science and Technology Agreement between Lomonosov Moscow State University, Skobeltsyn Institute of Nuclear Physics, and the University of Bristol.

Table 1

Atomic and Molecular Emissions Monitored in this Work, with the Argon Transitions Labelled using both Russell-Saunders and Paschen Notation.

Species	Transition	Monitored Wavelength / nm	Upper state energy / eV	Lower state energy / eV
H_2*	$d^3\Pi_u \rightarrow a^3\Sigma_g^+$	603.19	13.848 [#]	11.788 [#]
	$G^1\Sigma_g^+ \rightarrow B^1\Sigma_u^+$	463.14	13.863 [#]	11.183 [#]
H*	$n = 3 \rightarrow n = 2$	656.28	12.085	10.198
	$n = 4 \rightarrow n = 2$	486.13	12.748	10.198
	$n = 5 \rightarrow n = 2$	434.04	13.054	10.198
Ar*	$3p^5(^2P^o_{1/2})4p^1 \rightarrow 3p^5(^2P^o_{3/2})4s^1$ ($2p_2 \rightarrow 1s_5$)	696.54	13.327	11.548
	$3p^5(^2P^o_{3/2})4p^1 \rightarrow 3p^5(^2P^o_{3/2})4s^1$ ($2p_9 \rightarrow 1s_5$)	811.53	13.075	11.548
	$3p^5(^2P^o_{1/2})4p^1 \rightarrow 3p^5(^2P^o_{1/2})4s^1$ ($2p_2 \rightarrow 1s_2$)	826.45	13.327	11.828
Kr*	$4p^5(^2P^o_{3/2})6p^1 \rightarrow 4p^5(^2P^o_{3/2})5s^1$	427.40	12.815	9.915
	$4p^5(^2P^o_{3/2})6p^1 \rightarrow 4p^5(^2P^o_{3/2})5s^1$	431.96	12.784	9.915
	$4p^5(^2P^o_{3/2})6p^1 \rightarrow 4p^5(^2P^o_{3/2})5s^1$	437.61	12.864	10.032
Cu*	$3d^{10}4p^1 \rightarrow 3d^{10}4s$	324.75	3.816	0.000
	$3d^{10}4p^1 \rightarrow 3d^{10}4s$	327.40	3.785	0.000

[#] quoted term values are for the $v' = 0$ level, defined relative to X, $v'' = 0$ level.

Table 2.

Selected Reactions for Charged Species and for Emitting H*, H_2* and Ar* Neutrals. Ar($1s_{3,5}$) and Ar($1s_{2,4}$) Represent, Respectively, the Sums of the $1s_3$ and $1s_5$ (Lowest Metastable) and the $1s_2$ and $1s_4$ (Lowest Resonance) States of Ar. Ar(4p) Represents the Sum of $2p_i$ (i = 1-10) States with Excitation Energies in the Range 12.9-13.5 eV. Rate Coefficients k_i and Reaction Rates R_i for the Important Reactions Involving Charged and Electronically Excited Species are Presented for the Following Plasma Conditions Prevailing at r = 0, z = 3.5 mm: X_0(Ar) = 0.33 in H_2, along with ~10 ppm Air Impurity, $|E|/(N\times a)$ = 34 Td, p = 150 Torr, P = 1.5 kW, T_g = 2713 K, T_e = 1.57 eV, under which Conditions the Main Species Mixing Ratios are 8.3%H/18.8%Ar/H_2 (as for Figure 10 also). k_i are in Units of $cm^3\ s^{-1}$ Except for the Radiative Decay Reactions (s^{-1}), T_g is in K, and H_2 and Ar Denote the Respective Ground States. Table S3 Presents an Expanded Version of this Table, Including References to the Sources of the Rate Data.

Reaction			R_i / $cm^{-3}\ s^{-1}$
	Electron impact excitation	k_i / $cm^3\ s^{-1}$	
1	H(n=1) + e → H(n=2) + e	4.6×10^{-12}	5.9×10^{16}
2	H(n=1) + e → H(n=3) + e	7.6×10^{-14}	9.7×10^{14}
3	H(n=1) + e → H(n=4) + e	1.2×10^{-14}	1.6×10^{14}
4	H(n=1) + e → H(n=5) + e	3.4×10^{-15}	4.4×10^{13}
5	H(n=1) + e → H(n=6) + e	1.5×10^{-15}	2.0×10^{13}
6	H_2 + e → $H_2(b^3\Sigma_u^+)$ + e → 2H + e	2.2×10^{-11}	2.4×10^{18}
7	H_2 + e → $H_2(B^1\Sigma_u^+)$ + e	3.5×10^{-13}	3.9×10^{16}
8	H_2 + e → $H_2(c^3\Pi_u)$ + e	4.7×10^{-13}	5.3×10^{16}
9	H_2 + e → $H_2(a^3\Sigma_g^+)$ + e	7.5×10^{-13}	8.5×10^{16}
10	H_2 + e → $H_2(C^1\Pi_u)$ + e	5.1×10^{-14}	5.7×10^{15}
11	H_2 + e → $H_2(e^3\Sigma_u^+)$ + e	5.1×10^{-15}	5.7×10^{14}
12	H_2 + e → $H_2(d^3\Pi_u)$ + e	3.8×10^{-15}	4.3×10^{14}
13	H_2 + e → $H_2(G^1\Sigma_g^+)$ + e	1.6×10^{-15}	1.8×10^{14}
14	Ar + e → Ar($1s_{3,5}$) + e	2.2×10^{-13}	6.3×10^{15}

15	$Ar + e \rightarrow Ar(1s_{2,4}) + e$	1.5×10^{-13}	4.3×10^{15}
16	$Ar + e \rightarrow Ar(4p) + e$	4.8×10^{-14}	1.4×10^{15}
	Electron-ion dissociative recombination	k_i / cm^3 s^{-1}	
17	$H_3^+ + e \rightarrow H(n=2) + H_2$ (or $\rightarrow 3H$)	3.5×10^{-9}	2.2×10^{14}
18	$H_3O^+ + e \rightarrow OH^* + 2H$ (or $\rightarrow H_2O + H$)	9.6×10^{-9}	5.9×10^{13}
19	$ArH^+ + e \rightarrow Ar + H(n=2)$	2.2×10^{-10}	3.5×10^{12}
	Electron impact ionization	k_i / cm^3 s^{-1}	
20	$H(n=1) + e \rightarrow H^+ + e + e$	1.3×10^{-14}	1.6×10^{14}
21	$H_2 + e \rightarrow H_2^+ + e + e$	2.1×10^{-15}	2.4×10^{14}
22	$Ar + e \rightarrow Ar^+ + e + e$	1.5×10^{-15}	4.5×10^{13}
	Associative ionization	k_i / cm^3 s^{-1}	
23	$H(n=2) + H_2 \rightarrow H_3^+ + e$	$3.82\times10^{-8}/T_g^{0.95}$	1.3×10^{15}
24	$Ar(1s_{3,5})/Ar(1s_{2,4}) + H(n=1) \rightarrow ArH^+ + e$	10^{-11}	1.8×10^{14}
	Excitation transfer H* ↔ H_2*	k_i / cm^3 s^{-1}	
25	$H(n=3) + H_2 \rightarrow H(n=1) + H_2(a^3\Sigma_g^+)$	10^{-9}	6.7×10^{15}
–25	$H(n=1) + H_2(a^3\Sigma_g^+) \rightarrow H(n=3) + H_2$	3.3×10^{-10}	7.0×10^{15}
26	$H(n=6) + H_2 \rightarrow H(n=1) + H_2(e^3\Sigma_u^+)$	6.0×10^{-10}	3.5×10^{14}
–26	$H(n=1) + H_2(e^3\Sigma_u^+) \rightarrow H(n=6) + H_2$	7.9×10^{-10}	2.6×10^{14}
	Excitation transfer H* ↔ Ar*	k_i / cm^3 s^{-1}	
27	$H(n=3) + Ar \rightarrow H(n=1) + Ar(1s_{3,5})$	2.3×10^{-10}	4.0×10^{14}
–27	$H(n=1) + Ar(1s_{3,5}) \rightarrow H(n=3) + Ar$	2.4×10^{-11}	2.4×10^{14}
28	$H(n=3) + Ar \rightarrow H(n=1) + Ar(1s_{2,4})$	2.3×10^{-10}	4.0×10^{14}
–28	$H(n=1) + Ar(1s_{2,4}) \rightarrow H(n=3) + Ar$	4.9×10^{-11}	3.7×10^{14}
29	$Ar(1s_{3,5}) + H(n=1) \rightarrow Ar + H(n=2)$	2.0×10^{-10}	2.1×10^{15}
30	$Ar(1s_{2,4}) + H(n=1) \rightarrow Ar + H(n=2)$	2.5×10^{-11}	1.9×10^{14}
31	$Ar(4p) + H(n=1) \rightarrow Ar + H(n=6)$	3.0×10^{-11}	7.4×10^{13}
–31	$Ar + H(n=6) \rightarrow Ar(4p) + H(n=1)$	2.6×10^{-11}	3.8×10^{12}
	Excitation transfer Ar* ↔ H_2*	k_i / cm^3 s^{-1}	
32	$H_2(a^3\Sigma_g^+) + Ar \rightarrow H_2 + Ar(1s_{3,5})$	10^{-10}	4.7×10^{15}
–32	$Ar(1s_{3,5}) + H_2 \rightarrow Ar + H_2(a^3\Sigma_g^+)$	3.5×10^{-11}	3.2×10^{15}
33	$H_2(a^3\Sigma_g^+) + Ar \rightarrow H_2 + Ar(1s_{2,4})$	10^{-10}	4.7×10^{15}
–33	$Ar(1s_{2,4}) + H_2 \rightarrow Ar + H_2(a^3\Sigma_g^+)$	7.4×10^{-11}	4.8×10^{15}

34	$Ar(4p) + H_2 \rightarrow Ar + H_2(e^3\Sigma_u^+)$	2.0×10^{-11}	4.3×10^{14}
–34	$H_2(e^3\Sigma_u^+) + Ar \rightarrow H_2 + Ar(4p)$	3.0×10^{-10}	2.2×10^{14}
	Selected radiative transitions	k_i / s^{-1}	
35	$H(n=3) \rightarrow H(n=2) + h\nu$	4.4×10^{7}	7.6×10^{14}
36	$H_2(B^1\Sigma_u^+) \rightarrow H_2 + h\nu$	1.7×10^{9}	4.2×10^{16}
37	$H_2(a^3\Sigma_g^+) \rightarrow H_2(B^3\Sigma_u^+) + h\nu$	9.0×10^{7}	4.3×10^{16}
38	$Ar(4p) \rightarrow Ar(1s_{3,5})/Ar(1s_{2,4}) + h\nu$	2×10^{7}	1.1×10^{15}
	Reactive quenching	k_i / $cm^3\ s^{-1}$	
39	$Ar(1s_{3,5}) + H_2 \rightarrow Ar + 2H$	7.0×10^{-11}	6.4×10^{15}
40	$Ar(1s_{2,4}) + H_2 \rightarrow Ar + 2H$	7.0×10^{-11}	4.6×10^{15}
41	$H(n=2) + H_2 \rightarrow 3H$	10^{-9}	6.1×10^{16}
42	$H_2^* + H_2 \rightarrow 2H + H_2$	2.2×10^{-10}	9.7×10^{16}
	Ion conversions	k_i / $cm^3\ s^{-1}$	
43	$ArH^+ + H_2 \rightarrow H_3^+ + Ar$	6.3×10^{-10}	1.4×10^{19}
–43	$H_3^+ + Ar \rightarrow ArH^+ + H_2$	6.5×10^{-9} $\exp(-6830/T_g)$	1.4×10^{19}
44	$H_3^+ + H_2O \rightarrow H_3O^+ + H_2$	5.9×10^{-9}	1.4×10^{15}
–44	$H_3O^+ + H_2 \rightarrow H_3^+ + H_2O$	$2.3\times10^{-12}\times T_g\times$ $\exp(-29300/T_g)$	1.2×10^{15}
45	$ArH^+ + H_2O \rightarrow H_3O^+ + Ar$	8×10^{-10}	4.8×10^{13}
–45	$H_3O^+ + Ar \rightarrow ArH^+ + H_2O$	$7.4\times10^{-14}\times T_g^{1.4}\times$ $\exp(-34500/T_g)$	4.2×10^{13}

Figure Captions

Figure 1

Spatial profiles of (a) $I_{em}(H_2$, d–a, $v'=0–v''=0$, Q(3)), (b) $I_{em}(H_\alpha)$, (c) I_{em}(Ar*, 696.54 nm) and (d) I_{em}(Ar*, 811.53 nm) from a MW activated plasma for various X_0(Ar). The data in panels (a) and (b) were obtained by adding the appropriate F(Ar) to $F(H_2)$ = 300 sccm, while the data in (c) and (d) were obtained by increasing F(Ar) and setting $F(H_2)$ = {300 – F(Ar)} sccm. In all cases, p = 150 Torr and P = 1.5 kW. The relative intensities in plots (a) – (c) are displayed on a common vertical scale, whereas the profiles in (d) have been scaled to a common maximum peak intensity (which accounts for the noise on the low X_0(Ar) traces at higher z).

Figure 2

Plot showing the different trends in (a) $I_{em}(H_2*)$, (b) $I_{em}(H_\alpha)$ and (c) I_{em}(R*) with changes in X_0(R) for R = Ar (solid lines) and Kr (dashed lines). The displayed trends are for z = 2 and 7.5 mm (red and black symbols, respectively). The data in these panels have been normalised to (a) the $I_{em}(H_2*)$ signals at z = 2 mm and X_0(R) = 0, (b) the $I_{em}(H_\alpha)$ signals at z = 7.5 mm and X_0(R) = 0, and (c) the I_{em}(R*) signals measured at low z and highest X_0(R).

Figure 3

Spatial profiles of $I_{em}(H_2*)$, $I_{em}(H_\alpha)$ and I_{em}(Kr*, 431.96 nm) from a MW activated plasma for various X_0(Kr) obtained by increasing F(Kr) and setting $F(H_2)$ = {300 – F(Kr)} sccm, with p = 150 Torr and P = 1.5 kW. The relative intensities in each plot are displayed on a common vertical scale.

Figure 4

(a) Spatial profiles of I_{em}(Cu*, 324.75 nm) from a MW activated plasma for various X_0(Ar) measured by increasing F(Ar) and setting $F(H_2)$ = {300 – F(Ar)} sccm, with p = 150 Torr and P = 1.5 kW. The relative intensities are displayed on a common vertical scale. (b) Plot comparing the X_0(Ar) dependences of I_{em}(Cu*, 324.75 nm), measured at z = 2 and 7.5 mm, with the maximal intensity in each case normalised to unity. (c) semi-logarithmic plot comparing the X_0(Ar) dependences of I_{em}(Cu*, 324.75 nm) with the [ArH^+], [H_3^+] and [H_3O^+] concentrations close above the base plate at r = 18 mm predicted by the 2-D (r, z) modeling.

Figure 5

Normalized EEDFs ($f(\varepsilon)/\int f(\varepsilon)d\varepsilon$, plotted on a logarithmic scale) for a reduced electric field $|E|/(N\times a)$ ~33.4 Td, T_g = 2900 K, X(H) = 0.12 and various argon mole fractions, X(Ar). The respective electron temperatures T_e ~1.39-1.84 eV are shown in the inset (with T_{tail} ~0.76 eV in each case).

Figure 6

(a) Axial (at r = 0) and (b) radial (at z = 10.5 mm) profiles of the reduced electric fields, $|E|/(N\times a)$, the power density, $|jE|$, and the electron temperature T_e and T_{tail} for H_2/Ar mixtures containing, respectively, X_0(Ar) = 0.07 and 0.33 (filled and open symbols, respectively), under base conditions of p and P.

Figure 7

Radial profiles of [H], n_e and T_{gas} calculated at (a) z = 10.5 mm and (b) z = 0.5 mm (*i.e.* 0.5 mm above the substrate) for H_2/Ar mixtures with X_0(Ar) = 0, 0.07 and 0.33, under base conditions of p and P. The brown bar near the bottom of (b) indicates the radius of the substrate, while the orange and cyan bars at the top of (a) illustrate the radial extents of the H_2/Ar (X_0(Ar) = 0.07 and 0.33, respectively) plasma defined as the volume within which the concentrations of emitting species are within an order of magnitude of their maximal values.

Figure 8

Radial concentration profiles (at z = 10.5 mm) for selected species in H_2/Ar plasmas with X_0(Ar) = (a) 0.07 and (b) 0.33, with p = 150 Torr and P = 1.5 kW. The different $[H_3O^+]/[H_3^+]$ ratios in the two plots reflect the increased air contamination assumed in the X_0(Ar) = 0.33 modeling.

Figure 9

Axial concentration profiles (at r = 0) for selected species in H_2/Ar plasmas with X_0(Ar) = (a) 0.07 and (b) 0.33, with p = 150 Torr and P = 1.5 kW. As in Figure 9, the different $[H_3O^+]/[H_3^+]$ ratios in the two plots reflect the increased air contamination assumed in the X_0(Ar) = 0.33 modeling.

Figure 10

Histogram (logarithmic scale) showing the total electron impact excitation (EIE) and ionization (EII) rates of H, H_2 and Ar, the rates of the dominant excitation transfer (ET) processes between these species and the reactive quenching (RQ) and radiative (Rad) loss rates for all three species at $r = 0$, $z = 3.5$ mm, for the following plasma conditions: input gas mixture comprising X_0(Ar) = 0.33 in H_2, along with ~10 ppm air impurity, $|E|/(N \times a)$ = 34 Td, p = 150 Torr, P = 1.5 kW, T_g = 2713 K, T_e = 1.57 eV, under which conditions the main species mixing ratios are 8.3%H/18.8%Ar/H_2. Loss rates for H*, H_2* and Ar* are shown by negative going bars. For comparative purposes, the rate of electron impact dissociation (EID) of H_2 is also included, at the far left.

Figure 11

Comparisons of the calculated column densities (left hand axis, shown by filled symbols defined in the upper inset) and measured emission intensities (right hand axis, shown by lines, as defined in the lower panels) of (a) H(n = 3) atoms, (b) H_2(d, v = 0) molecules and (c) Ar(4p) atoms for H_2/Ar plasmas operating at p = 150 Torr, P = 1.5 kW with different X_0(Ar).

Figure 1

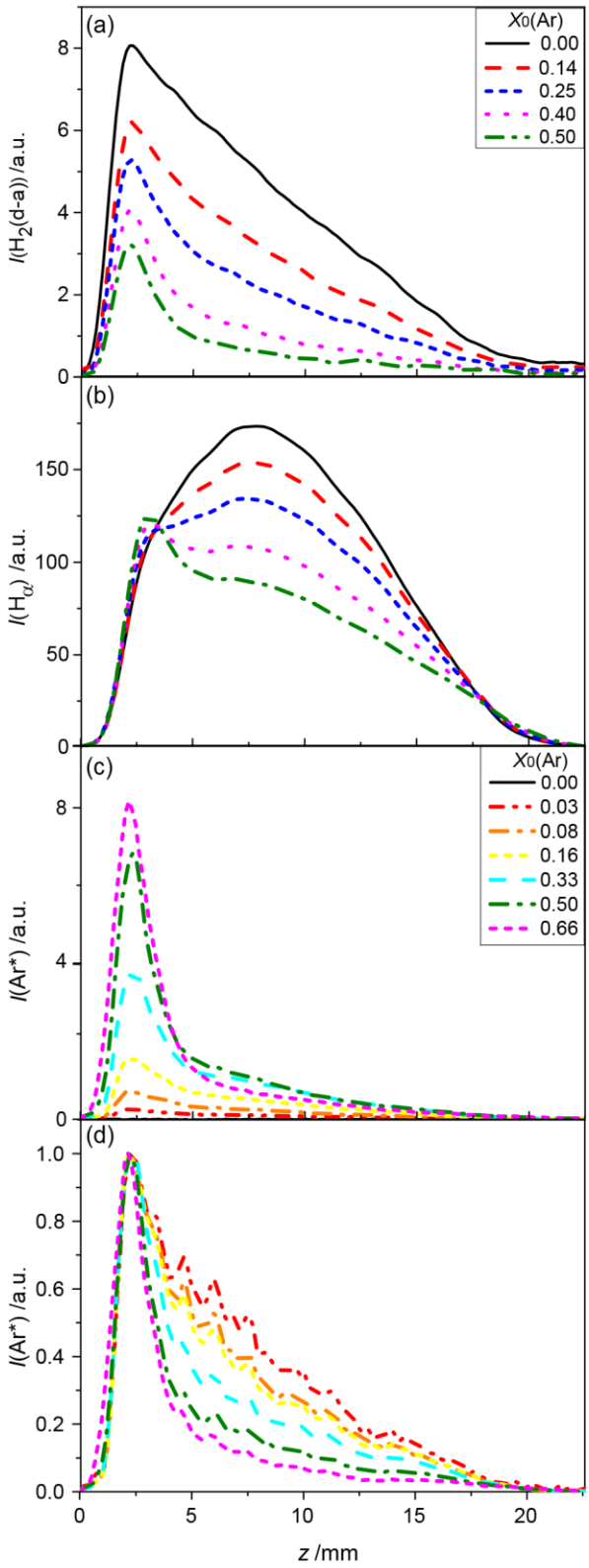
(a)
X0(Ar)
0.00
0.14
0.25
0.40
0.50
I(H2(d-a)) /a.u.
(b)
I(Hα) /a.u.
(c)
X0(Ar)
0.00
0.03
0.08
0.16
0.33
0.50
0.66
I(Ar*) /a.u.
(d)
I(Ar*) /a.u.
z /mm

Figure 2

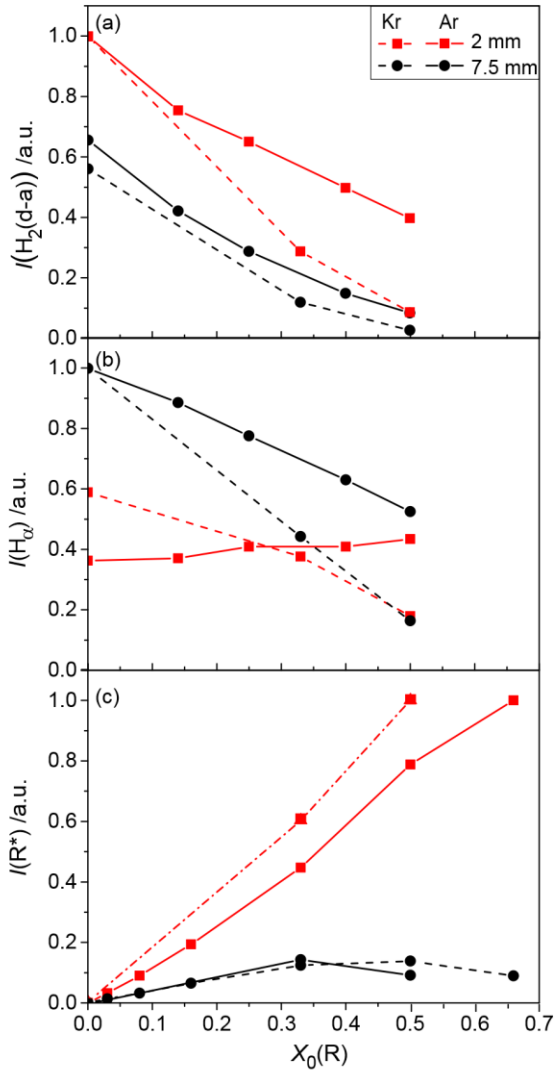

Figure 3

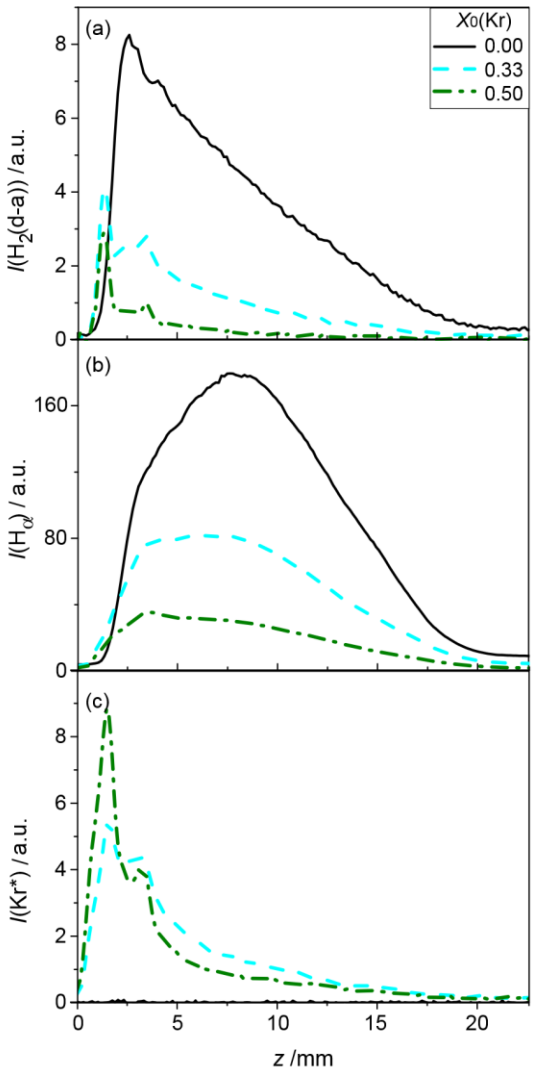

Figure 4

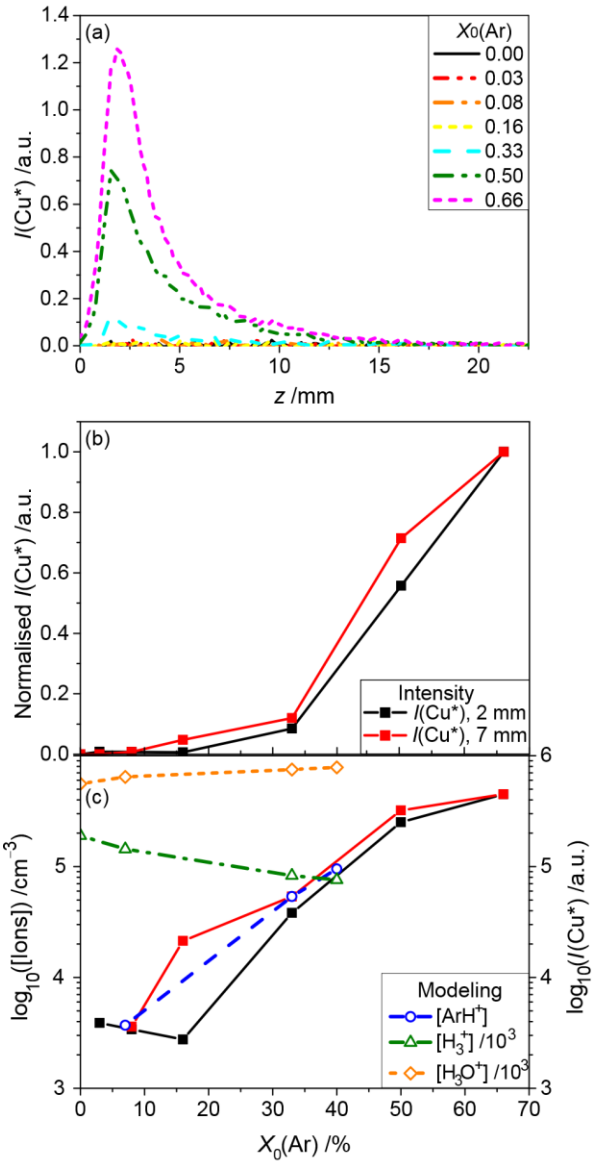
(a)
X0(Ar)
0.00
0.03
0.08
0.16
0.33
0.50
0.66
I(Cu*) /a.u.
z /mm
(b)
Normalised I(Cu*) /a.u.
Intensity
I(Cu*), 2 mm
I(Cu*), 7 mm
(c)
log10([Ions]) /cm-3
log10(I(Cu*) /a.u.)
Modeling
[ArH+]
[H3+] /10^3
[H3O+] /10^3
X0(Ar) /%

Figure 5

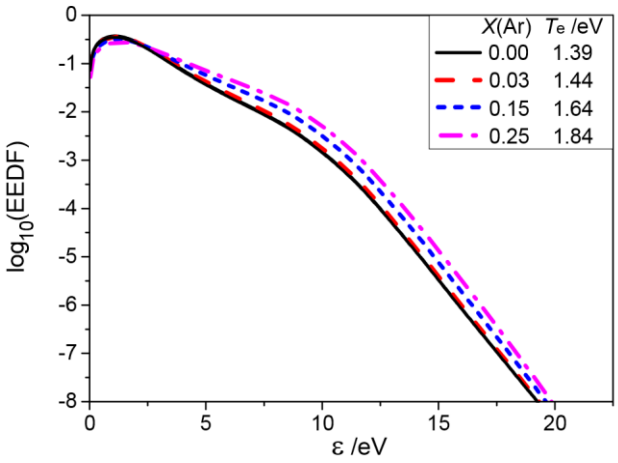
X(Ar) Te /eV
0.00 1.39
0.03 1.44
0.15 1.64
0.25 1.84
log10(EEDF)
ε /eV
0
-1
-2
-3
-4
-5
-6
-7
-8
0
5
10
15
20

Figure 6

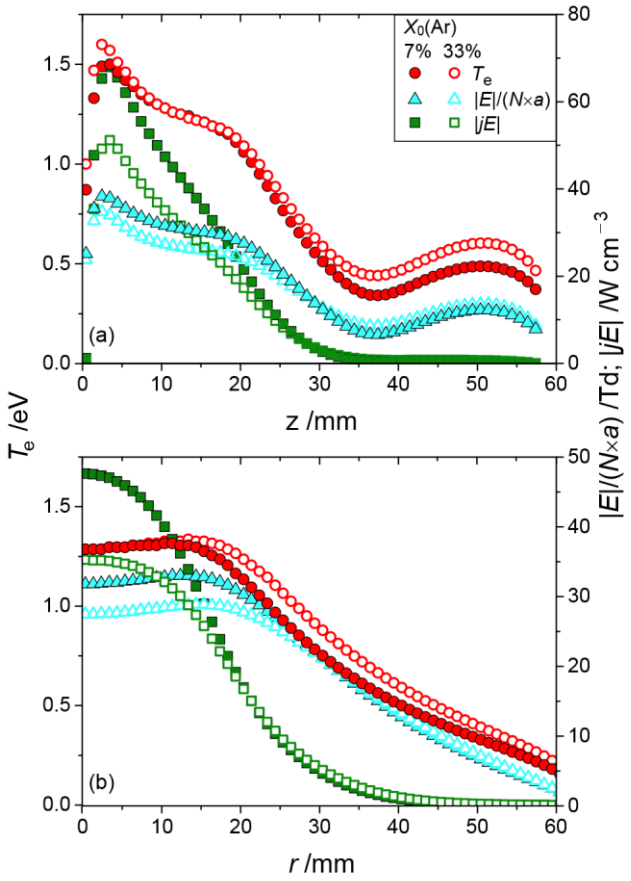

Figure 7

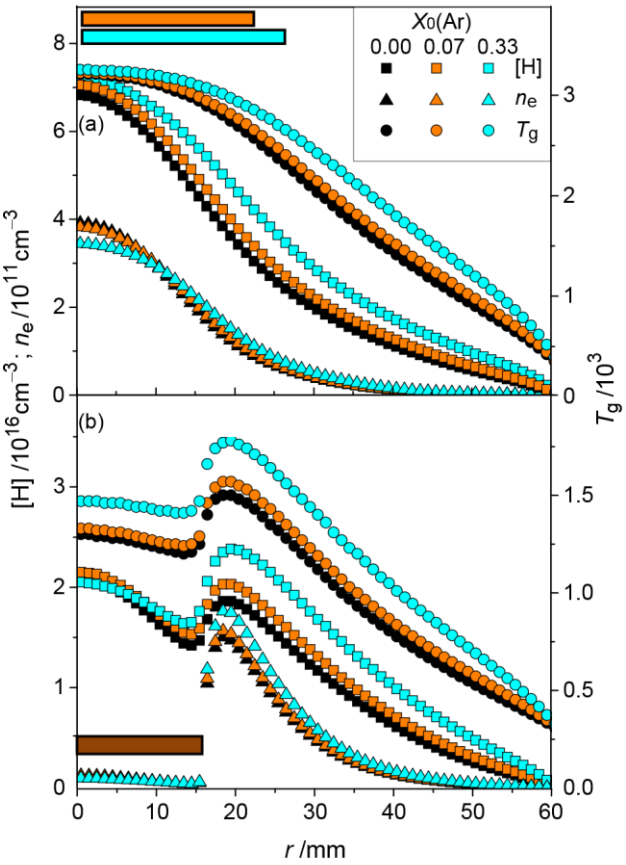

Figure 8

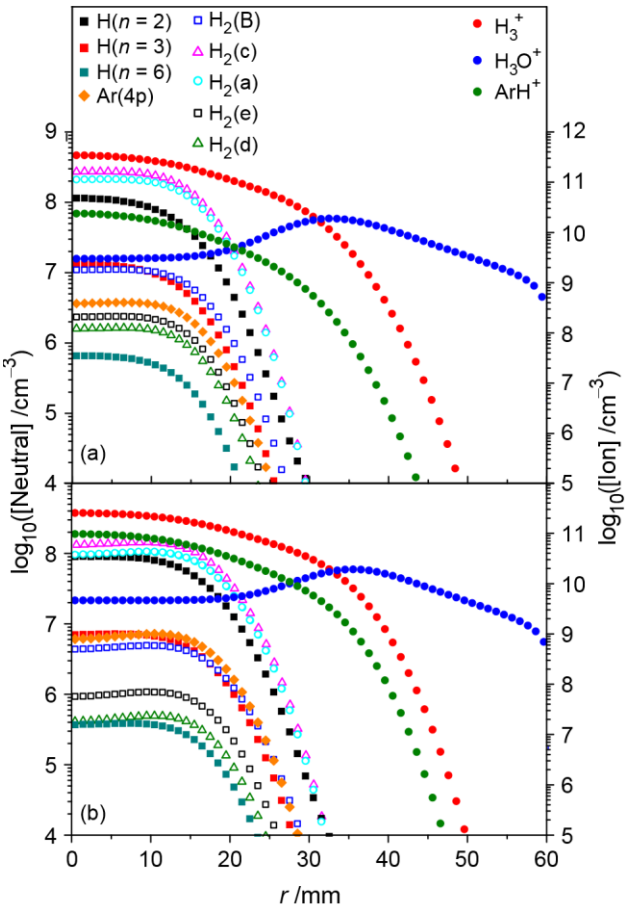
H(n = 2)
H(n = 3)
H(n = 6)
Ar(4p)
H2(B)
H2(c)
H2(a)
H2(e)
H2(d)
H3+
H3O+
ArH+
(a)
(b)
log10([Neutral] /cm−3)
log10([Ion] /cm−3)
r /mm

Figure 9

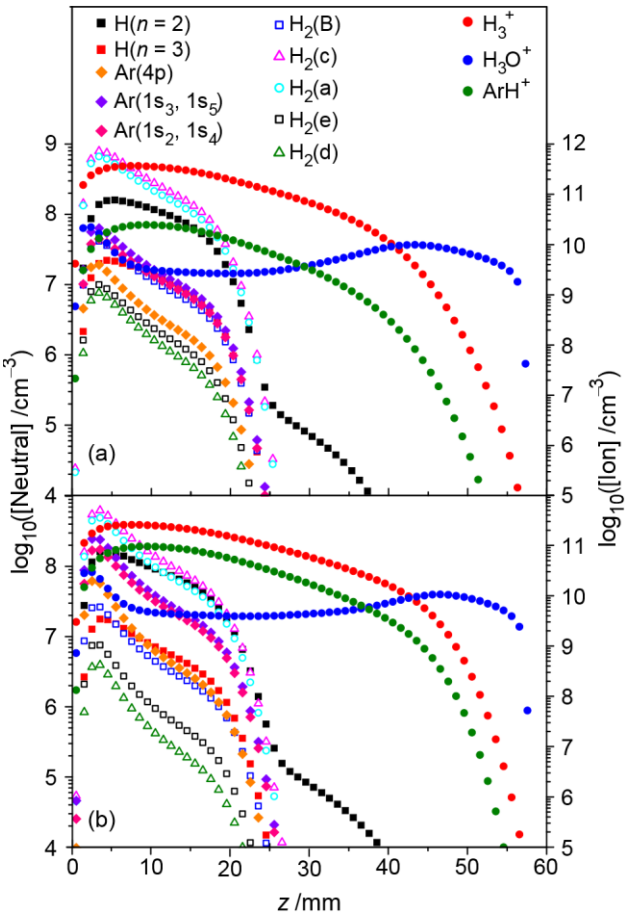
H(n = 2)
H(n = 3)
Ar(4p)
Ar(1s3, 1s5)
Ar(1s2, 1s4)
H2(B)
H2(c)
H2(a)
H2(e)
H2(d)
H3+
H3O+
ArH+
(a)
(b)
log10([Neutral] /cm−3)
log10([Ion] /cm−3)
z /mm

Figure 10

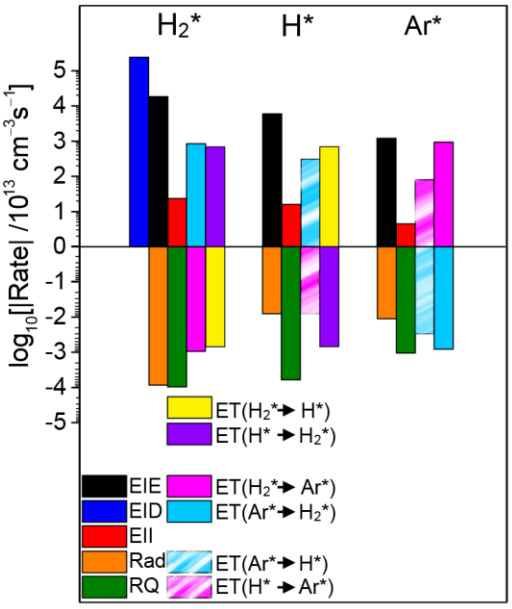
H2*
H*
Ar*
log10[|Rate| /10^13 cm^-3 s^-1]
5
4
3
2
1
0
-1
-2
-3
-4
-5
ET(H2* → H*)
ET(H* → H2*)
EIE
EID
EII
Rad
RQ
ET(H2* → Ar*)
ET(Ar* → H2*)
ET(Ar* → H*)
ET(H* → Ar*)

Figure 11

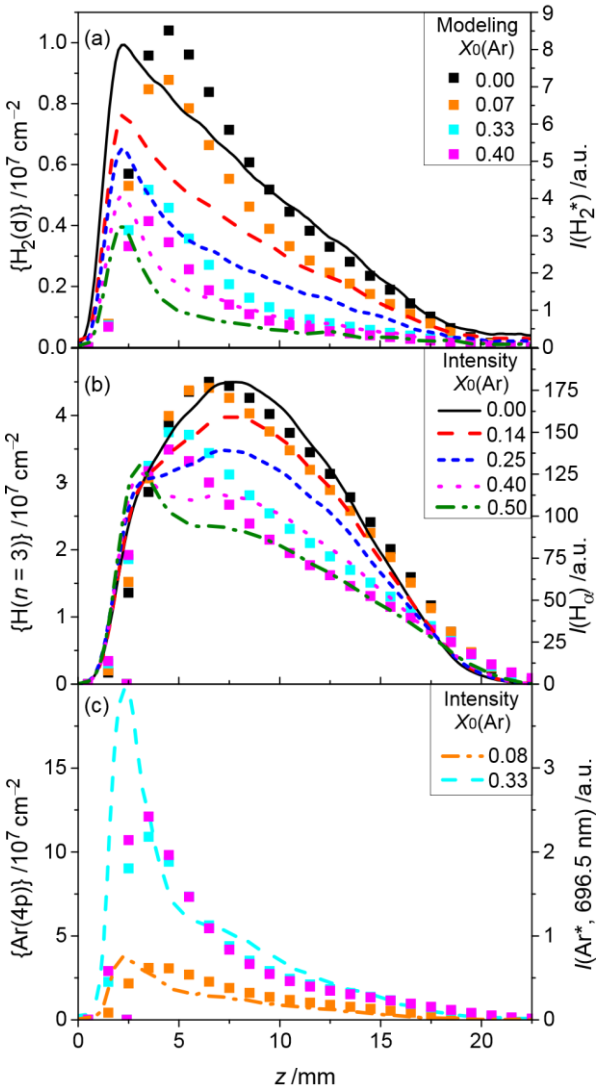
(a)
Modeling
X0(Ar)
0.00
0.07
0.33
0.40
{H2(d)} /10^7 cm^-2
I(H2*) /a.u.
(b)
Intensity
X0(Ar)
0.00
0.14
0.25
0.40
0.50
{H(n = 3)} /10^7 cm^-2
I(Hα) /a.u.
(c)
Intensity
X0(Ar)
0.08
0.33
{Ar(4p)} /10^7 cm^-2
I(Ar*, 696.5 nm) /a.u.
z /mm

References

[1] Goodwin, D.G.; Butler, J.E. In *Handbook of Industrial Diamonds and Diamond Films*; Prelas, M., Popovici, G., Bigelow, L.G., Eds.; Marcel Dekker; New York, 1998; pp. 527-581.

[2] Gicquel, A.; Hassouni, K.; Silva, F.; Achard, J. CVD Diamond Films: From Growth to Applications. *Curr. Appl. Phys*. **2001**, *1*, 479-496.

[3] Butler, J.E.; Mankelevich, Y.A. Cheesman, A.; Ma, J.; Ashfold, M.N.R. Understanding the Chemical Vapor Deposition of Diamond: Recent Progress. *J. Phys. Condens. Matter* **2009**, *21*, 364201.

[4] Hassouni, K.; Silva, F.; Gicquel, A. Modelling of Diamond Deposition Microwave Cavity Generated Plasmas. *J. Phys. D: Appl. Phys.* **2010**, *43*, 153001 and references therein.

[5] Zhu, W.; Inspektor, A.; Badzian, A.R.; McKenna, T.; Messier, R. Effects of Noble Gases on Diamond Deposition from Methane-Hydrogen Microwave Plasmas, *J. Appl. Phys.*, **1990**, *68*, 1489-1496.

[6] Han, Y.-S.; Kim. Y.-K.; Lee, J.-Y. Effects of Argon and Oxygen Addition to the CH_4-H_2 Feed Gas on Diamond Synthesis by Microwave Plasma Enhanced Chemical Vapor Deposition, *Thin Solid Films*, **1997**, *310*, 39-46.

[7] Shih, H.C.; Sung, C.P.; Fan, W.L. The effect of Noble Gases on the Formation of CVD Diamond Film, *Surf. Coat. Technol.*, **1992**, *54/55*, 380-386.

[8] Zhou, D.; Gruen, D.M.; Qin, L.C.; McCauley, T.G.; Krauss, A.R. Control of Diamond Film Microstructure by Ar Additions to CH_4/H_2 Microwave Plasmas, *J. Appl. Phys.*, **1998**, *84*, 1981-1989.

[9] Butler, J.E.; Sumant, A.V. The CVD of Nanodiamond Materials. *Chem. Vap. Deposn*. **2008**, *14*, 145-160, and references therein.

[10] Zhou, D.; McCauley, T.G.; Qin, L.C.; Krauss, A.R.; Gruen, D.M. Synthesis of Nanocrystalline Diamond Thin Films from an Ar-CH_4 Microwave Plasma, *J. Appl. Phys.*, **1998**, *83*, 540-543.

[11] Jiao, S.; Sumant, A.; Kirk, M.A.; Gruen, D.M.; Krauss, A.R.; Auciello, O. Microstructure of Ultrananocrystalline Diamond Films Grown by Microwave Ar-CH_4 Plasma Chemical Vapor Deposition With or Without Added H_2, *J. Appl. Phys.*, **2001**, *90*, 118-122.

[12] Gicquel, A.; Chenevier, M.; Hassouni, K.; Tserepi, A.; Dubus, M. Validation of Actinometry for Estimating Relative Hydrogen Atom Densities and Electron Energy

Evolution in Plasma Assisted Diamond Deposition Reactors. *J. Appl. Phys*. **1998**, *83*, 7504-7521.

[13] Geng, Z.C.; Xu, Y.; Yang, X.F.; Wang, W.G.; Zhu, A.M. Atomic Hydrogen Determination in Medium-Pressure Microwave Discharge Hydrogen Plasmas via Emission Actinometry. *Plasma Sources Sci. Technol*. **2005**, *14*, 76-82.

[14] Ma, J.; M.N.R. Ashfold, M.N.R.; Mankelevich, Yu.A.; Validating Optical Emission Spectroscopy as a Diagnostic of Microwave Activated $CH_4/Ar/H_2$ Plasmas used for Diamond Chemical Vapor Deposition, *J. Appl. Phys.*, **2009**, *105*, 043302.

[15] Derkaoui, N.; Rond, C.; Gries, T.; Henrion, G.; Gicquel, A. Determining Electron Temperature and Electron Density in Moderate Pressure H_2/CH_4 Microwave Plasma. *J. Phys. D. Appl. Phys*. **2014**, *47*, 205201.

[16] Hayashi, F.; Uyama, H.; Matsumoto, O. Effect of Dilution Gases in Methane on the Deposition of Diamond-Like Carbon in a Microwave Discharge. III: Effect of Rare Gases, *Thin Solid Films*, **1990**, *189***,** 313-319.

[17] Fox, O.J.L.; Ma, J.; May, P.W.; Ashfold, M.N.R.; Mankelevich, Yu.A., The Role of Inert Gas in MW-Enhanced Plasmas for the Deposition of Nanocrystalline Diamond Thin Films, *Diam. Rel. Mater.*, **2009**, *18*, 750-758.

[18] Richley, J.C.; Fox, O.J.L.; Ashfold, M.N.R.; Mankelevich, Yu.A. Combined Experimental and Modeling Studies of Microwave Activated $CH_4/H_2/Ar$ Plasmas for Microcrystalline, Nanocrystalline, and Ultrananocrystalline Diamond Deposition, *J. Appl. Phys*., **2011**, *109***,** 063307.

[19] Tallaire, A.; Rond, C.; Bénédic, F.; Brinza, O.; Achard, J.; Silva, F.; Gicquel, A. Effect of Argon Addition on the Growth of Thick Single Crystal Diamond by High-Power Plasma CVD, *Phys. Status Solidi A*, **2011**, *208*, 2028-2032.

[20] Mahoney, E.J.D.; Truscott, B.S.; Ashfold, M.N.R.; Mankelevich, Yu.A. Optical Emission from C_2^- Anions in Microwave-Activated CH_4/H_2 Plasmas for Chemical Vapor Deposition of Diamond, *J. Phys. Chem. A*, **2017**, *121***,** 2760-2772.

[21] Yamada, H.; Chayahara, A.; Mokuno, Y. Effect of Ar Addition on Uniformity of Diamond Growth by using Microwave Plasma Chemical Vapor Deposition. *Diam. Rel. Mater*. **2018**, *87*, 143-148.

[22] Mahoney, E.J.D.; Truscott, B.S.; Mushtaq, S.; M.N.R. Ashfold, M.N.R.; Mankelevich, Yu.A. Spatially Resolved Optical Emission and Modelling Studies of Microwave-Activated

Hydrogen Plasmas Operating under Conditions Relevant for Diamond Chemical Vapor Deposition, *J. Phys. Chem. A,* **2018**, *122*, 8286-8300.

[23] Paul, R.; Srivastava, I.B. Mutual Diffusion of the Gas Pairs H_2–Ne, H_2–Ar, and H_2–Xe at Different Temperatures. *J. Chem. Phys*. **1961**, *35*, 1621-1624.

[24] Khouw, B.; Morgan, J.E.; Schiff, H.I. Experimental Measurements of the Diffusion Coefficients of H Atoms in H_2 and in H_2–He and H_2–Ar Mixtures. *J. Chem. Phys*. **1969**, *50*, 66-70.

[25] Dandy, D.S.; Coltrin, M.E. A Simplified Analytical Model of Diamond Growth in Direct Current Arcjet Reactors. *J. Mater. Res*. **1995**, *10*, 1993-2010.

[26] Mankelevich, Yu.A.; Ashfold, M.N.R.; Ma, J. Plasma-Chemical Processes in Microwave Plasma-Enhanced Chemical Vapour Deposition Reactors Operating with C/H/Ar Gas Mixtures. *J. Appl. Phys*. **2008**, *104*, 113304.

[27] Carbone, E.; van Dijk, J.; Kroesen, G. Experimental Evidence of Resonant Energy Collisional Transfers between Argon 1s and 2p States and Ground State H Atoms by Laser Collisional Induced Fluorescence. *Plasma Sources Sci. Technol.* **2015**, *24*, 025036.

[28] Zhu, Xi-M.; Vaskov Tsankov, T.; Luggenhölscher, D.; Czarnetzki, U. 2D Collisional-Radiative Model for Non-Uniform Argon Plasmas: With or Without 'Escape Factor'. *J. Phys. D: Appl. Phys.* **2015**, *48*, 085201.

[29] Lishawa, C.R.; Feldstein, J.W.; Stewart, T.N.; Muschlitz, E.E. Excitation of Continuum Radiation in Collisions of (1) Electrons and (2) Metastable Argon Atoms with H_2 and D_2. *J. Chem. Phys*. **1985**, *83*, 133-139.

[30] Jimenez-Redondo, M.; Cueto, M.; Domenech, J.L.; Tanarro, I.; Herrero, V.J. Ion Kinetics in Ar/H_2 Cold Plasmas: The Relevance of ArH^+. *RSC Adv*., **2014**, *4*, 62030-62041.

[31] Bogaerts, A.M.; Gijbels, R. Effects of Adding Hydrogen to an Argon Glow Discharge: Overview of Relevant Processes and some Qualitative Explanations. *J. Anal. At. Spectrom*., **2000**, *15*, 441-449.

[32] Chilton, J.E.; Boffard, J.B.; Schappe, R.S.; Lin, C.C. Measurement of Electron-Impact Excitation into the $3p^5 4p$ Levels of Argon using Fourier-transform Spectroscopy. *Phys. Rev. A*, **1998**, *57*, 267-277.

[33] Gargioni, E.; Grosswendt, B. Electron Scattering from Argon: Data Evaluation and Consistency. *Rev. Mod. Phys.* **2008**, *80*, 451-480.

[34] Voloshin, D.G.; Mankelevich, Yu.A.; Proshina, O.V.; Rakhimova, T.V. Modeling of Single and Dual Frequency Capacitive Discharge in Argon Hydrogen Mixture. Dynamic Effects and Ion Energy Distribution Functions. Plasma Proc. and Polymers, **2017**, *14*, 1600119.

[35] Goos, E.; Burcat, A.; Ruscic, B. Extended Third Millenium Ideal Gas Thermochemical Database with Updates from Active Thermochemical Tables. <http://burcat.technion.ac.il/dir>; 5 Oct. 2016, mirrored at http://garfield.chem.elte.hu/Burcat/burcat.html (accessed 8 February 2019).

[36] Larsson, M.; McCall, B.J.; Orel, A.E. The Dissociative Recombination of H_3^+ – A Saga Coming to an End? *Chem. Phys. Lett*. **2008**, *462*, 145-151.

[37] Neau, A.; Al Khalili, A.; Rosén, S.; Le Padellec, A.; Derkatch, A.M.; Shi, W.; Vikor, L.; Larsson, M.; Semaniak, J.; Thomas, R.; *et al*. Dissociative Recombination of D_3O^+ and H_3O^+: Absolute Cross Sections and Branching Ratios. *J. Chem. Phys*. **2000**, *113*, 1762-1770.

[38] Mitchell, J.B.A.; Novotny, O.; LeGarrec, J.L.; Florescu-Mitchell, A.; Rebrion-Rowe, C.; Stolyarov, A.V.; Child, M.S.; Svendsen, A.; El Ghazaly, M.A.; Andersen, L.H. Dissociative Recombination of Rare Gas Hydride Ions: II. ArH^+. *J. Phys. B: At. Mol. Opt. Phys*. **2005**, *38*, L175-L181.

[39] Florescu-Mitchell, A.I.; Mitchell, J.B.A. Dissociative Recombination. *Phys. Reports*. **2006**, *430*, 277-374.

[40] Fortov, V.E. (ed.) Encyclopedia of Low Temperature Plasma. Nauka: Moscow, **2000**, Vol. 1.

[41] Schilke, P.; Neufeld, D.A.; Müller, H.S.P.; Comito, C.; Bergin, E.A.; Lis, D.C.; Gerin, M.; Black, J.H.; Wolfire, M.; Indriolo, N.; *et al*. Ubiquitous Argonium (ArH^+) in the Diffuse Interstellar Medium: A Molecular Tracer of Almost Purely Atomic Gas. *Astron. Astrophys*. **2014**, *566*, A29.

[42] Payzant, J.D.; Schiff, H.I.; Bohme, D.K. Determination of the Proton Affinity from the Kinetics of Proton Transfer Reactions. V. The Equilibrium $H_3^+ + Kr \leftrightarrow KrH^+ + H_2$ and the Relative Proton Affinity of Kr and H_2. *J. Chem. Phys*. **1975**, *63*, 149-153.

[43] Hopf, C.; von Keudell, A.; Jacob, W. Chemical Sputtering of Hydrocarbon Films. *J. Appl. Phys*., **2003**, *94*, 2373-2380.

[44] Wu, F.Y.; Levitin, G.; Hess, D.W. Low-Temperature Etching of Cu by Hydrogen-Based Plasmas. *ACS Appl. Mater. Interfaces* **2010**, *2*, 2175-2179.